



Insight into the boosted catalytic performance and chlorine resistance of nanosphere-like meso-macroporous $\text{CrO}_x/\text{MnCo}_3\text{O}_x$ for 1,2-dichloroethane destruction



Mingjiao Tian^{a,1}, Xu Guo^{a,1}, Rui Dong^a, Zheng Guo^a, Jianwen Shi^b, Yanke Yu^c, Mingxing Cheng^a, Reem Albilali^d, Chi He^{a,e,*}

^a State Key Laboratory of Multiphase Flow in Power Engineering, School of Energy and Power Engineering, Xi'an Jiaotong University, Xi'an, 710049, Shaanxi, PR China

^b Center of Nanomaterials for Renewable Energy, State Key Laboratory of Electrical Insulation and Power Equipment, School of Electrical Engineering, Xi'an Jiaotong University, Xi'an, 710049, Shaanxi, China

^c Department of Chemical Engineering, Columbia University, New York, 10027, United States

^d Department of Chemistry, College of Science, Imam Abdulrahman Bin Faisal University, P.O. Box 1982, Dammam, 31441, Saudi Arabia

^e National Engineering Laboratory for VOCs Pollution Control Material & Technology, University of Chinese Academy of Sciences, Beijing, 101408, PR China

ARTICLE INFO

Keywords:

Catalytic destruction
 $\text{CrO}_x/\text{MnCo}_3\text{O}_x$ composite
 1,2-dichloroethane
 Stability
 Reaction mechanism

ABSTRACT

Catalyst chlorine poisoning is a critical issue to be solved for chlorine-containing VOCs decomposition. Herein, we found that three-dimensional nanosphere-like meso-macroporous MnCo_3O_x (SMC-F) synthesized via a co-precipitation method has much higher activity and selectivity for 1,2-dichloroethane destruction than the bulk MnCo_3O_x ; however, polychlorinated by-products as 1,1,2-trichloroethane, trichloroethylene, perchloroethylene, trichloromethane and perchloromethane originated from the cleavage of C–Cl and C–C bonds can be detected. As such, CrO_x was further introduced to enhance the low temperature activity and selectivity of SMC-F. Results reveal that the incorporation of CrO_x boosts surface lattice oxygen (O^{2-}) amount and mobility and generates highly reducible Cr^{6+} and Mn^{4+} species in Cr/SMC-F, improving its activity and selectivity remarkably. Only 1,1,2-trichloroethane can be found during 1,2-dichloroethane destruction as the C–C bond cleavage route is generally inhibited over Cr/SMC-F. The improved O^{2-} mobility and oxidation property of Cr/SMC-F facilitate surface Cl desorption, ensuring its superior catalytic efficiency and chlorine resistance.

1. Introduction

Urbanization and industrialization contribute to rapidly increasing emissions of volatile organic compounds (VOCs), which are major contributors to the formation of secondary pollutants and photochemical smog. Chlorine-containing VOCs (CVOCs) are considered as a class of important pollutants for the environment and human beings due to their strong bioaccumulation potential, acute toxicity and resistance to degradation. The economic and efficient elimination of CVOCs has caught great attention of researchers in recent years [1–3]. Different technologies have been commonly investigated, which include adsorption/absorption, photocatalysis, catalytic oxidation, thermal oxidation and plasma oxidation [4]. Among these, catalytic oxidation is recognized as one of the most promising candidates for the removal of CVOCs attributing to its low operating temperature,

controllable reaction selectivity and high activity and stability [5,6].

Highly efficient catalyst system plays a decisive role in CVOC destruction. The catalysts for CVOC oxidation mainly include noble metal supported materials [7], zeolites/modified zeolites [8], perovskites [9] and metal oxides [10]. In general, the noble metal based catalysts exhibit satisfactory catalytic activity at low temperature, but they are easily attacked by Cl species, leading to the loss of active species and subsequent deactivation of catalysts. Moreover, the formation of secondary polychlorinated pollutants with tremendous toxicity is another issue to be solved in the destruction of CVOCs over noble metal supported materials. In addition to this, the high cost of noble metal materials could also limit its practical applications. Similarly, zeolites/modified zeolites also face with the problem of producing polychlorinated hydrocarbon by-products and suffer from obvious coke-induced deactivation in connection with their strong acidity and poor

* Corresponding author at: State Key Laboratory of Multiphase Flow in Power Engineering, School of Energy and Power Engineering, Xi'an Jiaotong University, Xi'an, 710049, Shaanxi, PR China.

E-mail address: chi_he@xjtu.edu.cn (C. He).

¹ These authors are contributed equally to this work.

oxidizing ability [10]. Perovskite-type oxides are one kind of potential catalysts for CVOC oxidation owing to their low costs, high structure and thermal stability; however, they are less active and always need very high operation temperature to achieve a total CVOC conversion, which greatly limit their vast application [6]. Comparatively, transition metal (e.g., V, Cr, Mn, Co, Cu, Zn, and Fe) oxides have the advantageous of adjustable catalytic activity, superior resistance to Cl-poisoning and coking, and wide availability [5,11]. Amongst, Co-based materials are considered to be one type of efficient catalysts for the oxidation of CVOCs because of the existence of Co^{2+} at tetrahedral sites and Co^{3+} at octahedral sites in Co_3O_4 that can promote the interaction between cobalt and replacement element [10,12]. It is reported that the appropriate replacement of Co with other elements can obtain higher catalytic activity and thermal stability than the single oxides [13]. In particular, Co-Mn oxides have attracted much attention due to their remarkable low temperature catalytic performance [14]. Tang et al. [15] reported that Co-Mn mixed oxide shows an improved activity for ethyl acetate and *n*-hexane oxidation compared to the single MnO_x or Co_3O_4 material because the strong synergistic effect of Mn and Co species makes a great contribution to its low temperature reducibility. Similarly, Alphonse et al. [16] claimed that the $\text{Co}_{2.3}\text{Mn}_{0.7}\text{O}_4$ composite catalyst has a better propane oxidation activity than the single cobalt oxide. Cai et al. [10] found that the substitution of Co^{3+} at octahedral sites in Co_3O_4 structure by Mn species can increase Co^{2+} concentration on catalyst surface, which can promote 1,2-dichlorobenzene oxidation. However, large amounts of reaction by-products are usually formed over Co-based catalysts during catalytic decomposition of CVOCs, which would poison the catalyst easily [10]. It is declared that the Cr-containing oxides are highly active and selective materials for CVOC destruction and the formation of toxic by-products can be well controlled [6]. However, the use of CrO_x with inherent toxicity and the loss of Cr at high temperature should be reduced or avoided by confining low content Cr species in a robust structure. Therefore, it can be anticipated that the composite oxides which combine the merits of CrO_x and MnCo_3O_x would be a kind of promising materials for CVOC efficient destruction. Additionally, González-Prior et al. [17] proved that the activity of a catalyst is essentially related to its surface area and porous structure. A three-dimensional (3D) porous architecture with improved transportation and diffusion property of gas phase molecules has been demonstrated to be an efficient structure for the oxidation of VOCs [9].

In the present work, a 3D nanosphere-like meso-macroporous $\text{CrO}_x/\text{MnCo}_3\text{O}_x$ (Cr/SMC-F) composite catalyst was prepared and adopted in deep oxidation of 1,2-dichloroethane (1,2-DCE, a typical CVOC and model pollutant). The catalytic activity, by-products distribution and catalytic stability of synthesized materials were studied. Following this, the physicochemical properties of the fresh and used catalysts were systematically investigated to explore the intrinsic factors that determine the catalytic performance (activity, selectivity and stability) in 1,2-DCE oxidation. Finally, the 1,2-DCE destruction mechanism over prepared catalysts was further studied and proposed.

2. Experimental

2.1. Catalyst preparation

The 3D nanosphere-like meso-macroporous MnCo_3O_x was synthesized using a co-precipitation method. In a typical process, 0.4 g of KMnO_4 was dissolved in 400 mL of deionized water under vigorous stirring and heated to 70 °C for 1 h. 2.0 g of $\text{Co}(\text{NO}_3)_2 \cdot 6\text{H}_2\text{O}$ was dissolved in 10 mL of deionized water under vigorous stirring for 30 min. Thereafter, the obtained $\text{Co}(\text{NO}_3)_2$ solution was added dropwise into the aforementioned KMnO_4 solution at 70 °C and the mixture kept vigorous stirring for 1 h. The obtained paste was filtered, washed with deionized for several times, dried overnight at 60 °C, and then calcined at 450 °C for 3 h in air with a heating rate of 1 °C min⁻¹. The obtained

black powder was named SMC-F. Cr/SMC-F material was synthesized by a rotary evaporation method. Typically, 0.4 g of $\text{Cr}(\text{NO}_3)_3 \cdot 9\text{H}_2\text{O}$ was firstly dissolved in 60 mL of deionized water under vigorous stirring for 10 min and 1.0 g of the prepared SMC-F was then added into the $\text{Cr}(\text{NO}_3)_3$ solution under stirring for 10 min. Followed this, the solvent was removed by rotary evaporation at 70 °C with a rotate speed of 70 rpm min⁻¹. The obtained powder was dried at 80 °C for 10 h and then calcined at 450 °C for 3 h in air with a heating rate of 1 °C min⁻¹. The Cr/SMC-F material with a theoretical CrO_x loading of 5.2 wt.% was finally obtained (the practical Cr loading (4.3 wt.%) was measured by XRF, as shown in Table S3). For comparison, the bulk MnCo_3O_x (BMC-F) was also prepared using a sol-gel method. In a typical synthesis process, the stoichiometric amounts of $\text{Co}(\text{NO}_3)_2 \cdot 6\text{H}_2\text{O}$ and Mn (CH_3COO)₂·4H₂O were dissolved in 20 mL of deionized water under vigorous stirring at 60 °C for 15 min. 8.82 g of citric acid was added into the mixed solution until the formation of a transparent solution. The obtained sol was dried at 100 °C for 12 h and then calcined at 450 °C for 3 h in air with a heating rate of 1 °C min⁻¹. In addition, Cr/BMC-F material as a comparison catalyst was prepared using the similar synthesis route as Cr/SMC-F sample and bulk Co_3O_4 (BCo-F) was also prepared using the sol-gel method similar with BMC-F without Mn (CH_3COO)₂·4H₂O. Bulk CrO_x (BCr-F) was synthesized by calcination the corresponding metal precursors at 450 °C for 3 h. The catalysts after the stability tests are denoted as SMC-U, Cr/SMC-U, BMC-U and BCr-U, respectively.

2.2. Catalyst characterizations

Catalyst characterization were carried out by X-ray diffraction (XRD), Fourier transform infrared spectra (FTIR), X-ray photoelectron spectroscopy (XPS), field-emission scanning electron microscopy (FE-SEM), transmission electron microscopy (TEM), high-angle annular dark-field scanning-TEM (HAADF-STEM), X-ray energy spectrum analysis (EDS), low-temperature nitrogen-sorption, hydrogen temperature programmed reduction (H_2 -TPR), temperature-programmed desorption of oxygen or NH_3 (O_2 - or NH_3 -TPD), FT-IR spectroscopy for NH_3 adsorption (NH_3 -IR) and pyridine adsorption (Py-IR), thermo-gravimetric analysis (TG) of the used catalysts and *in situ* diffuse reflectance infrared spectroscopy (*in situ* DRIFTS) of prepared catalysts after pre-treating in N_2 at 400 °C for 1 h, similar to the methods reported by our group previously [8,9,18–23]. Temperature-programmed oxidation of the used catalysts (O_2 -TPO, after stability tests at 266 or 297 °C for 21 h) was carried out in a U-type quartz tube equipped with a portable mass spectrograph (SHP8400 PMS-L). The materials were heated from 50 to 800 °C in 30 mL min⁻¹ air flow with a heating rate of 10 °C min⁻¹ [23,24].

2.3. Catalytic activity

1,2-DCE catalytic destruction over prepared materials was conducted in a continuous flow quartz tube reactor (I.D. = 10 mm), in which the temperature was controlled by a K-type thermocouple placed in the catalyst bed. 0.5 g of the prepared material (40–60 mesh) and 1000 ppm of 1,2-DCE in a 300 mL min⁻¹ air stream (21 vol.% O_2 , N_2 balance) were used in each test (GHSV (gas hourly space velocity) of 36,000 mL g⁻¹ h⁻¹). The concentrations of 1,2-DCE and reaction products were analyzed by an online gas chromatograph (GC9890, China) equipped with an electron capture detector (ECD) and flame ionization detector (FID). HCl and Cl_2 concentrations were tested by a on-line HCl and Cl_2 detector (PN-2000, China). The 1,2-DCE conversion and CO , CO_2 , HCl and Cl_2 yields were calculated as follows:

The 1,2-DCE ($X_{1,2\text{-DCE}}$) conversion was calculated by Eq. (1):

$$X_{1,2\text{-DCE}} = \frac{C_{\text{in}} - C_{\text{out}}}{C_{\text{in}}} \times 100\% \quad (1)$$

where C_{in} and C_{out} are the inlet and outlet 1,2-DCE concentrations,

respectively.

The CO, CO₂, HCl and Cl₂ yields (denoted as Y_{CO} , Y_{CO_2} , Y_{HCl} and Y_{Cl_2} , respectively) were calculated by Eqs. (2)–(5), respectively:

$$Y_{CO} = \frac{C_{CO}}{2C_{in} \times X_{1,2-DCE}} \times 100\% \quad (2)$$

$$Y_{CO_2} = \frac{C_{CO_2}}{2C_{in} \times X_{1,2-DCE}} \times 100\% \quad (3)$$

$$Y_{HCl} = \frac{C_{HCl}}{2C_{in} \times X_{1,2-DCE}} \times 100\% \quad (4)$$

$$Y_{Cl_2} = \frac{C_{Cl_2}}{C_{in} \times X_{1,2-DCE}} \times 100\% \quad (5)$$

where C_{CO} , C_{CO_2} , C_{HCl} and C_{Cl_2} are the outlet CO, CO₂, HCl, Cl₂ concentrations, respectively. The stability tests were carried out at the corresponding temperature after a heating processing for 1,2-DCE destruction. In order to investigate multi-component pollutants effect on catalytic activity of the material, the time-on-stream experiments for 1,2-DCE oxidation were also carried out in the presence and absence of toluene or methanol.

3. Results and discussion

3.1. Structural and textural properties

The characteristic diffraction peaks centered at 19.0°, 31.3°, 36.9°, 44.9°, 59.5° and 65.2° can be respectively assigned to the (111), (220), (311), (400), (511) and (440) lattice planes, indicating the formation of cubic Co₃O₄ crystallites (JCPDS No. 01-076-1802) (Fig. S1). The main diffraction peaks of SMC-F locate at the same positions as the diffraction peaks of Co₃O₄ (36.9° and 65.2°), while the weak diffraction peaks of Mn₂O₃ (23.1°, 45.2° and 55.2°) and Mn₃O₄ (50.8°) can be also observed, which suggest that Co₃O₄, Mn₂O₃ and Mn₃O₄ phase exist in SMC-F mixed oxides (Figs. 1A and S1B). Compared to the diffraction peaks of Co₃O₄ material, the peaks of BMC-F mixed oxides shift to lower values of Bragg angles (18.8°, 30.9°, 36.7°, 44.4°, 58.7° and 65.4°), indicating that part of Mn species can enter into the cubic Co₃O₄ crystallites forming Mn_xCo_yO₂ solid solution; besides, Mn₂O₃, Mn₃O₄ and CoMn₂O₄ phases are also detected in BMC-F material (Figs. 1A and S1C). All diffraction peaks over BCr-F centered at 20 of 24.6°, 33.8°, 36.3°, 41.6°, 50.4°, 54.9°, 63.7° and 65.3° are in well agreement with the standard Cr₂O₃ (JCPDS No. 00-001-1294). It should be noted that no Cr₂O₃ diffraction peaks can be observed over Cr/SMC-F, suggesting that the formed crystallites are smaller than the detection limit and/or high dispersion of Cr species [25].

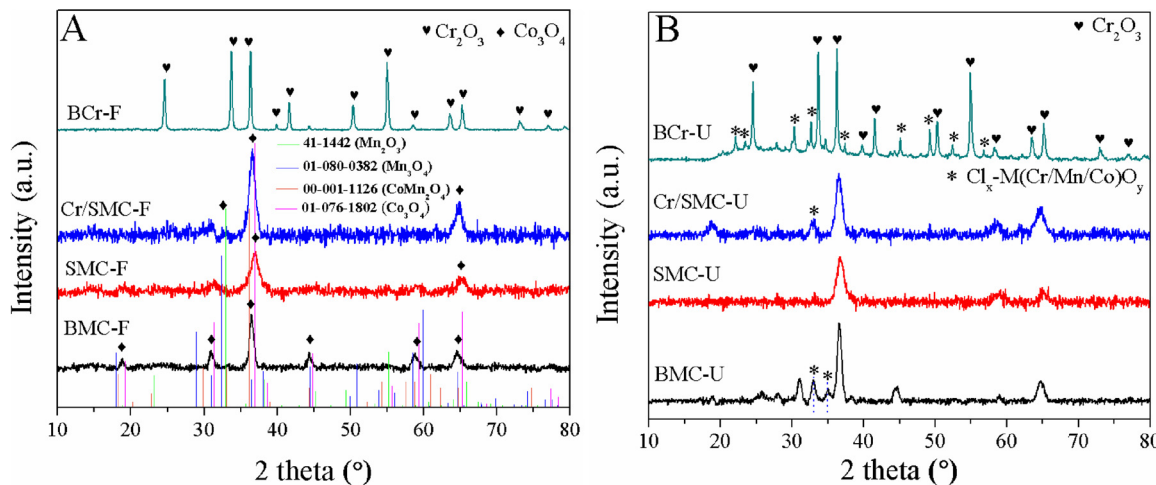
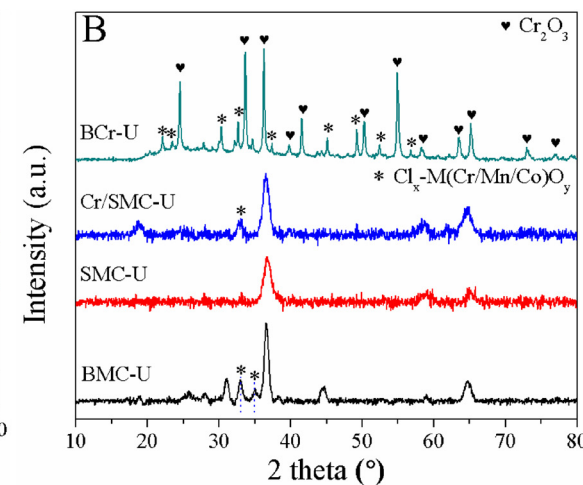


Fig. 1. XRD profiles of the (A) fresh and (B) used catalysts.

The surface property of the catalysts was studied by FTIR spectra, as shown in Fig. 2. The stretching vibrations in the range of 3500–3000 cm⁻¹ are attributed to the surface hydroxyl groups (–OH) over catalysts. The bands observed at around 1631 cm⁻¹ over all materials are corresponded to the C=O vibration of carbonyl and carboxyl groups [26,27]. The vibrations of Cr⁶⁺-O and Cr³⁺-O bonds are respectively located at the range of 1500–800 cm⁻¹ and 800–500 cm⁻¹ interval [28]. Compared to BCr-F sample with Cr⁶⁺-O vibration at 977 cm⁻¹, the Cr⁶⁺-O bond vibration over Cr/SMC-F shifts to a lower wavenumber of 938 cm⁻¹, suggesting the presence of interaction between CrO_x and SMC-F. The peaks at about 563 and 668 cm⁻¹ over BMC-F and SMC-F samples are normally attributed to the stretching vibration of octahedrally coordinated Co³⁺-O bond and tetrahedrally coordinated Co²⁺-O bond in the Co₃O₄ spinel lattice, respectively [29]. No changes of Co³⁺-O and Co²⁺-O bonds can be found in the FTIR spectra of BMC-F and SMC-F samples. Besides, the characteristic bands of Mn–O/Mn–O–Mn vibrations are not detected over all Mn-containing materials.

Typical FE-SEM patterns of prepared catalysts are displayed in Fig. 3a–l. It can be observed that BMC-F sample is composed of crumb-like particles with a large degree of porosity (Fig. 3a, b). The SMC-F and Cr/SMC-F catalysts have a regular 3D nanosphere-like porous morphology with an average diameter of about 240 nm (Fig. 3d–e and g–h). Such structure may promote the diffusion of reactant and product, enhance the anti-poisoning/cooking ability and subsequently improve the reaction stability of catalyst. BCr-F sample displays an irregular cubic-like morphology with an average diameter of around 200 nm (Fig. 3j,k). Fig. 3m–aa depicts the TEM, HAADF-STEM and EDS images of SMC-F and Cr/SMC-F catalysts. SMC-F nanosphere constructed by numerous nanorods has a diameter of around 232 nm (Fig. 3m), in accordance with the FE-SEM results (Fig. S2). The measured lattice distances of 0.284 and 0.242 nm over SMC-F nanosphere correspond to the (323) and (311) lattice planes of Mn₂O₃ and Co₃O₄, respectively (Fig. 3n). Fig. 3t, u shows the structure of nanosphere-like Cr/SMC-F catalyst, which is composed of SMC-F carrier and supported CrO_x nanocrystallites. The lattice spacing of 0.242, 0.284 and 0.247 nm is ascribed to the (311), (323) and (110) crystal planes of Co₃O₄, Mn₂O₃ and Cr₂O₃, respectively, in consistent with the XRD results (Fig. 1A). The EDS images indicate that the Mn, Co and O elements are homogeneously distributed over SMC-F sample (Fig. 3p–s) and similar situation of Mn, Co, Cr and O elements can be also found over Cr/SMC-F material (Fig. 3w–aa).

Fig. 4 shows the nitrogen adsorption-desorption isotherms and BJH pore size distribution of synthesized materials. The overlap of adsorption and desorption isotherms of BCr-F and BMC-F materials in relative pressure (P/P_0) < 0.8 is attributed to the multilayer adsorption



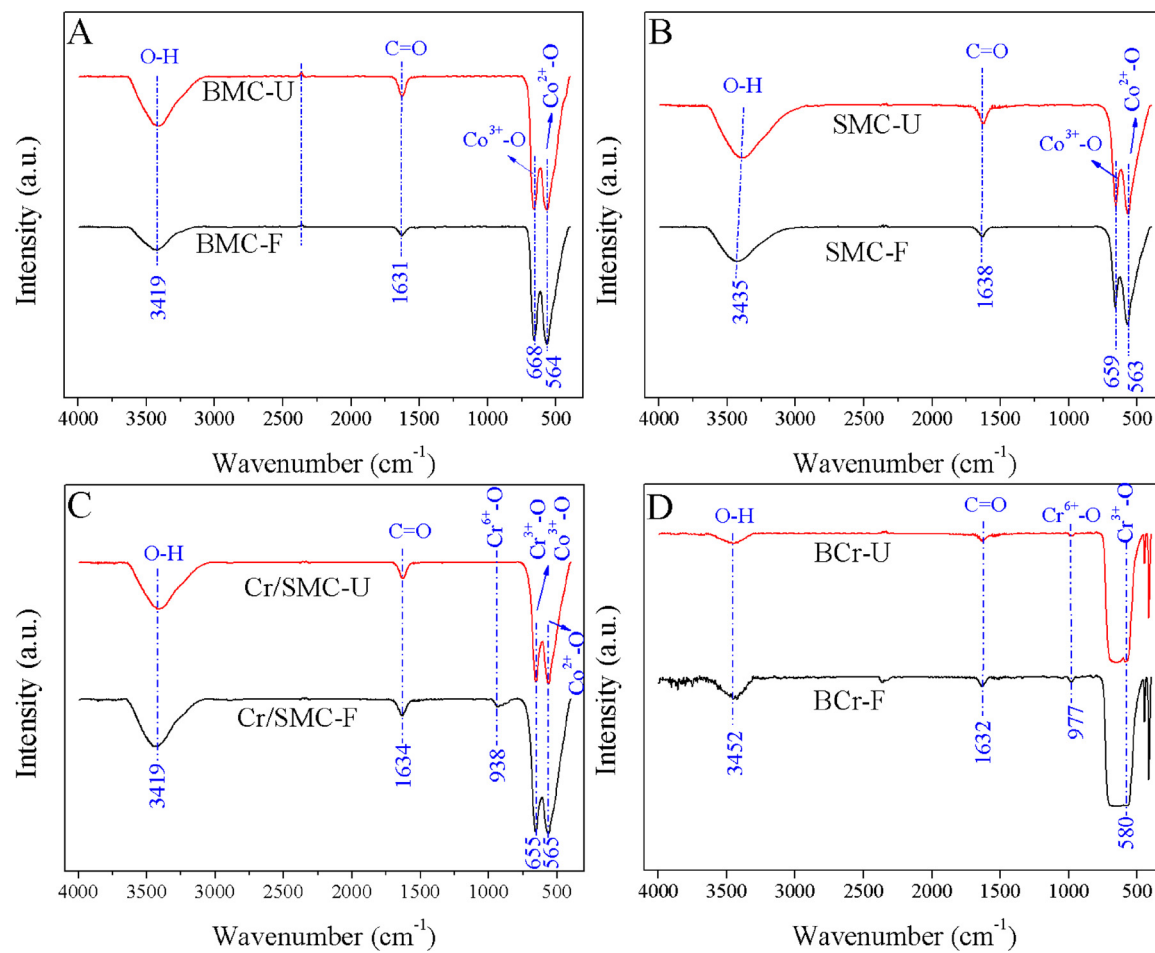


Fig. 2. FTIR spectra of the fresh and used catalysts.

(Fig. 4A), indicating that the two samples are nonporous or macroporous materials [30]. In addition to this, both the BCr-F and BMC-F catalysts display a type II isotherm with H3 type hysteresis loops at $P/P_0 = 0.9\text{--}1.0$, demonstrating the existence of a macroporous structure in the materials [31]. The isotherms of SMC-F and Cr/SMC-F exhibit a sharp increase at $P/P_0 < 0.1$, characteristic of the presence of structural micropores [32]. Besides, these two samples display a similar type IV isotherm with H2 ($P/P_0 = 0.4\text{--}0.9$) and H3 ($P/P_0 = 0.9\text{--}1.0$) hysteresis loops, indicating the co-existence of mesopores and macropores [33,34]. Interestingly, the H3 hysteresis loop of Cr/SMC-F at $P/P_0 = 0.9\text{--}1.0$ are obviously larger than that of SMC-F, which suggests that the introduction of CrO_x results in the formation of macropores [31]. It can be detected in Fig. 4B that BMC-F, SMC-F and Cr/SMC-F samples have a wide pore size distribution in pore diameter range of 2–40 nm and the average pore diameter follows the order of BMC-F (20.0 nm) > SMC-F (10.6 nm) > Cr/SMC-F (6.8 nm). A pore size distribution of BCr-F and Cr/SMC-F in pore diameter range of 100–120 nm corresponding to the macroporous structure can be found, in well agreement with the results of nitrogen adsorption-desorption isotherms (Fig. 4A). As shown in Table 1, the specific surface areas of all catalysts follow the order of BCr-F ($6.7 \text{ m}^2 \text{ g}^{-1}$) < BMC-F ($38.8 \text{ m}^2 \text{ g}^{-1}$) < Cr/SMC-F ($52.4 \text{ m}^2 \text{ g}^{-1}$) < SMC-F ($79.7 \text{ m}^2 \text{ g}^{-1}$). Compared with the BMC-F catalyst, the SMC-F sample possesses a much higher specific surface area owing to the presence of large amount of structural mesopores. The specific surface area of SMC-F sample has a significant decrease (ca. 34.2%) after introduction of CrO_x probably due to the enlarged average pore size and lessened micropore pore volume after doping of CrO_x (Table 1).

3.2. Surface composition and element status

As shown in Fig. 5, the Mn 2p XPS spectra can be split into Mn 2p_{3/2} and Mn 2p_{1/2} with binding energies (BEs) at 641.9 and 653.7 eV, respectively, in accordance with the previous work [8]. XPS spectra of Mn 2p_{3/2} suggests the co-existence of Mn^{3+} (BE = 641.4 eV) and Mn^{4+} (BE = 643.0 eV) species over all the prepared catalysts [35]. The $\text{Mn}^{4+}/\text{Mn}^{3+}$ ratios (Table 2) in the fresh catalysts respectively obey the sequence of BMC-F (1.21) < SMC-F (1.32) < Cr/SMC-F (1.35). It can be observed that the SMC-F owns more Mn^{4+} species than that of BMC-F and the introduction of CrO_x further enhances the ratio of Mn^{4+} species, which is beneficial for promoting catalytic activity [36]. The Co 2p_{3/2} (780.2 eV) and Co 2p_{1/2} (795.6 eV) XPS spectra with a BE separation of 15.4 eV demonstrate the presence of Co_3O_4 spinel phase, in agreement with the XRD results (Fig. 1) [12]. Co 2p_{3/2} can be deconvoluted into two components with BEs centered at 779.8 and 781.1 eV, assigning to the Co^{3+} and Co^{2+} , respectively [37]. Similarly, Co 2p_{1/2} can also be deconvoluted into two species with BEs of 794.8 (Co^{3+}) and 796.1 eV (Co^{2+}). As documented in Table 2, the fitting ratios of $\text{Co}^{3+}/\text{Co}^{2+}$ over SMC-F (1.81) and Cr/SMC-F (1.83) samples are higher than that of BMC-F (1.74), which suggest SMC-F and Cr/SMC-F own more oxide species than BMC-F. The Cr 2p_{3/2} spectra display three types of Cr species ($\text{Cr}(\text{OH})_3/\text{Cr}_2\text{O}_3$, Cr^{3+} and Cr^{6+}) with BEs centered at 575.5, 576.7 and 578.6 eV, respectively. Cr 2p_{1/2} XPS spectra show two distinct peaks associated with Cr^{3+} (585.9 eV) and Cr^{6+} (587.8 eV) in Cr/SMC-F material. The $\text{Cr}^{6+}/(\text{Cr}^{3+} + \text{Cr}_2\text{O}_3)$ ratio over Cr/SMC-F sample (0.62) is higher than that of BCr-F (0.58), suggesting that the strong interaction between chromium clusters and SMC-F support is beneficial for the formation of Cr^{6+} species.

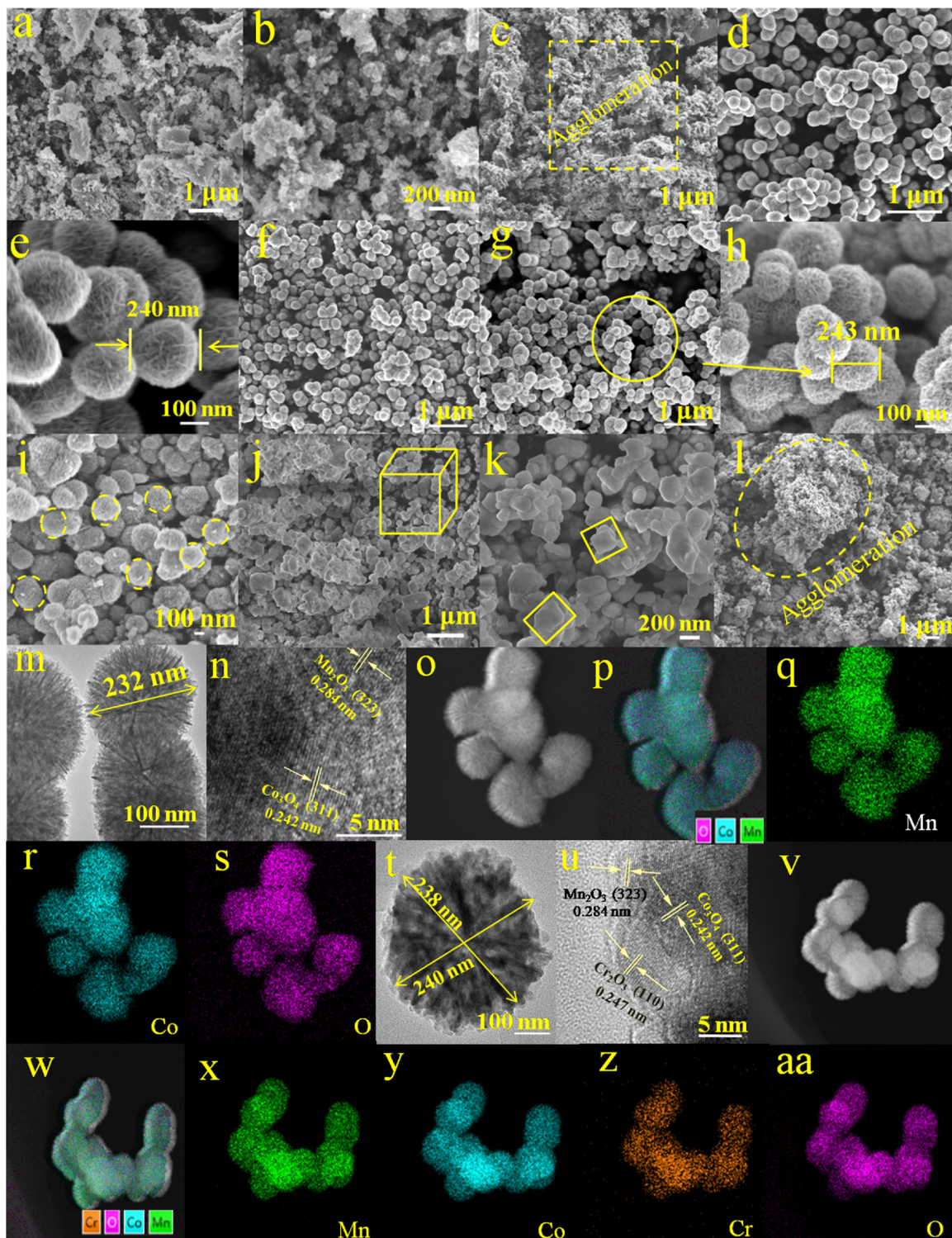


Fig. 3. FE-SEM images of (a,b) BMC-F, (c) BMC-U, (d,e) SMC-F, (f) SMC-U, (g,h) Cr/SMC-F, (i) Cr/SMC-U, (j,k) BCr-F and (l) BCr-U; HR-TEM patterns of (m,n) SMC-F and (t,u) Cr/SMC-F; EDS elemental mappings of (p-s) SMC-F and (w-aa) Cr/SMC-F derived from the STEM images of o and v, respectively.

O 1s XPS spectra of the samples can be deconvoluted into three peaks centered at 530.0, 531.6 and 533.0 eV, which are associated with the surface lattice oxygen species (O_{latt}), surface adsorbed oxygen species (O_{surf}) and the absorbed H_2O or CO_2 on the catalysts surface, respectively [38]. As shown in Table 2, the O_{latt}/O_{surf} ratio of SMC-F (1.85) is about 12 times higher than that of the BMC-F ($O_{latt}/O_{surf} = 0.15$) and the presence of Cr species obviously decrease the O_{latt}/O_{surf} ratio over Cr/SMC-F sample (0.77) because of the “ $O \rightarrow Cr$ ”

electron-transfer [10]. The O_{latt}/O_{surf} ratio of BCr-F is 0.91. It is reported that high concentration of active oxygen species is beneficial to improve the catalytic activity of the materials in CVOC oxidation process [8].

3.3. Reducibility and oxygen species mobility

The reducibility of the prepared catalysts was studied by H_2 -TPR. As

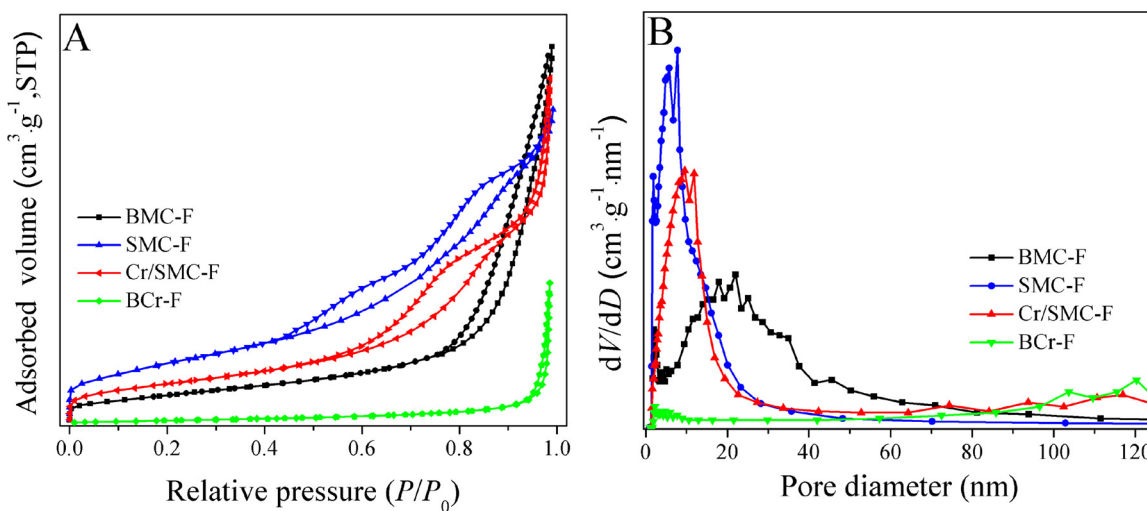


Fig. 4. (A) Nitrogen adsorption-desorption isotherms and (B) pore size distribution of prepared materials.

Table 1

Textural property and catalytic performance of synthesized catalysts.

Sample	$S_{\text{BET}}^{\text{a}}$ ($\text{m}^2 \text{g}^{-1}$)	V_t^{b} ($\times 10^{-2}$, $\text{cm}^3 \text{g}^{-1}$)	V_m^{c} ($\times 10^{-3}$, $\text{cm}^3 \text{g}^{-1}$)	D_p^{d} (nm)	T_{50}^{e} (°C)	T_{90}^{e} (°C)	E_a^{f} (kJ mol^{-1})
BMC-F	38.8	20.07	16.83	10.3	293	339	42.4
SMC-F	79.7	16.73	34.09	4.2	272	296	24.4
Cr/SMC-F	52.4	18.39	22.59	7.0	177	266	23.6
BCr-F	6.7	7.57	2.92	22.6	300	345	25.5

^a Specific surface area obtained at $P/P_0 = 0.05\text{--}0.30$.

^b Total pore volume estimated at $P/P_0 = 0.99$.

^c Microporous pore volume estimated by the *t*-plot method.

^d BJH pore diameter calculated from the N_2 desorption branch.

^e Temperatures at which 50% and 90% conversion of 1,2-DCE.

^f Apparent activation energy obtained from the Arrhenius plots.

displayed in Fig. 6A, two main reduction peaks centered at 278 and 408 °C can be observed over BCr-F sample, which is attributed to the reduction of Cr^{6+} to Cr^{3+} and highly dispersed Cr_2O_3 along with surface oxygen species, respectively [39]. The BMC-F, SMC-F and Cr/SMC-F materials show three main reduction peaks centered at the temperature range of 278–286 (R1), 370–391 (R2) and 509–580 °C (R3), respectively. The first peak in R1 region below 300 °C can be attributed to the reduction of surface oxygen and/or Co_3O_4 to CoO . The second peak in R2 region belongs to the reduction of CoO to metallic Co and Mn_2O_3 into Mn_3O_4 [40,41], and the third peak in R3 region can be assigned to the reduction of Mn_3O_4 to MnO and CoO to metallic Co [8,9]. However, H_2 consumption obtained from H_2 -TPR profiles reveals that the active components of the samples are not fully reduced in the process (Table S2). Fig. 6A shows that the first reduction peaks over the Cr/SMC-F and SMC-F catalysts shift toward the lower temperature side (275–278 °C) compared with that of the BMC-F sample (288 °C) due to the excellent low temperature catalytic activity of SMC-F. By comparing the H_2 consumption and the slope of H_2 -TPR curves (Table S2 and Fig. 6A), we can observe that H_2 consumption (R1, 2.04 mmol g^{-1}) and H_2 consumption rate of Cr/SMC-F are much higher than that of SMC-F (R1, 1.69 mmol g^{-1}) in temperature range of 220–270 °C, suggesting that Cr/SMC-F sample owns better reducibility than that of SMC-F at low temperature as the strong interaction between CrO_x and SMC-F promotes the formation of highly reducible Cr^{6+} species [42]. According to the H_2 consumption of the samples, the reducibility of the materials follows the order of Cr/SMC-F > SMC-F > BMC-F > BCr-F.

The property of active oxygen species over synthesized materials was characterized by O_2 -TPD, as shown in Fig. 6B. In general, desorption temperature of oxygen species follows the order of surface physically adsorbed oxygen (O_2 , < 200 °C) < surface chemisorbed

oxygen species (O_2^- and O^- , 200–500 °C) < surface lattice oxygen/lattice oxygen in bulk (O^{2-} , > 500 °C) [43]. Fig. 6B indicates that there are three types of oxygen species over BMC-F, SMC-F and Cr/SMC-F materials. For BMC-F, the O_2 desorption peaks centered at 111 and 425 °C are associated with O_2 (ads) and O_2^-/O^- (ads), respectively. SMC-F has the O_2 (ads), O_2^-/O^- (ads) and O^{2-} (ads) peaks at temperatures of 147, 459 and 601 °C, respectively. Similarly, the desorption peaks of O_2 (ads), O_2^- (ads)/ O^- (ads) and O^{2-} (ads) can be respectively observed at the temperature of 116, 447 and 590 °C over Cr/SMC-F (Fig. 6B). However, only the desorption peak of O^{2-} (ads) can be detected over the BCr-F sample at 626 °C. The corresponding areas of all O_2 desorption peaks are listed in Table S2. SMC-F owns better chemisorbed oxygen mobility than Cr/SMC-F and BMC-F materials because of its big chemisorbed oxygen desorption peak area (0.270). The area of surface lattice oxygen over Cr/SMC-F (0.231) is higher than that of SMC-F (0.162) indicating that the introduction of CrO_x promotes the mobility of surface lattice oxygen.

3.4. Surface acidity

Acidic property plays a key role in CVOC catalytic destruction, especially in CVOC molecule adsorption and cracking of C-Cl bonds [44]. The surface acidity of the prepared catalysts was systematically studied by using NH_3 -TPD and NH_3 -IR (Fig. 7). The acidic sites are generally divided into weak acidity (< 200 °C), moderate acidity (200–300 °C), strong acidity (300–450 °C) and super-strong acidic sites (450–600 °C) (The peak of NH_3 desorption within 450–600 °C is tentatively assume super-strong acidic sites here) [45]. As shown in Fig. 7A, SMC-F and Cr/SMC-F display a peak in the range from 50 to 300 °C, which associates with the desorption of NH_3 adsorbed on metal

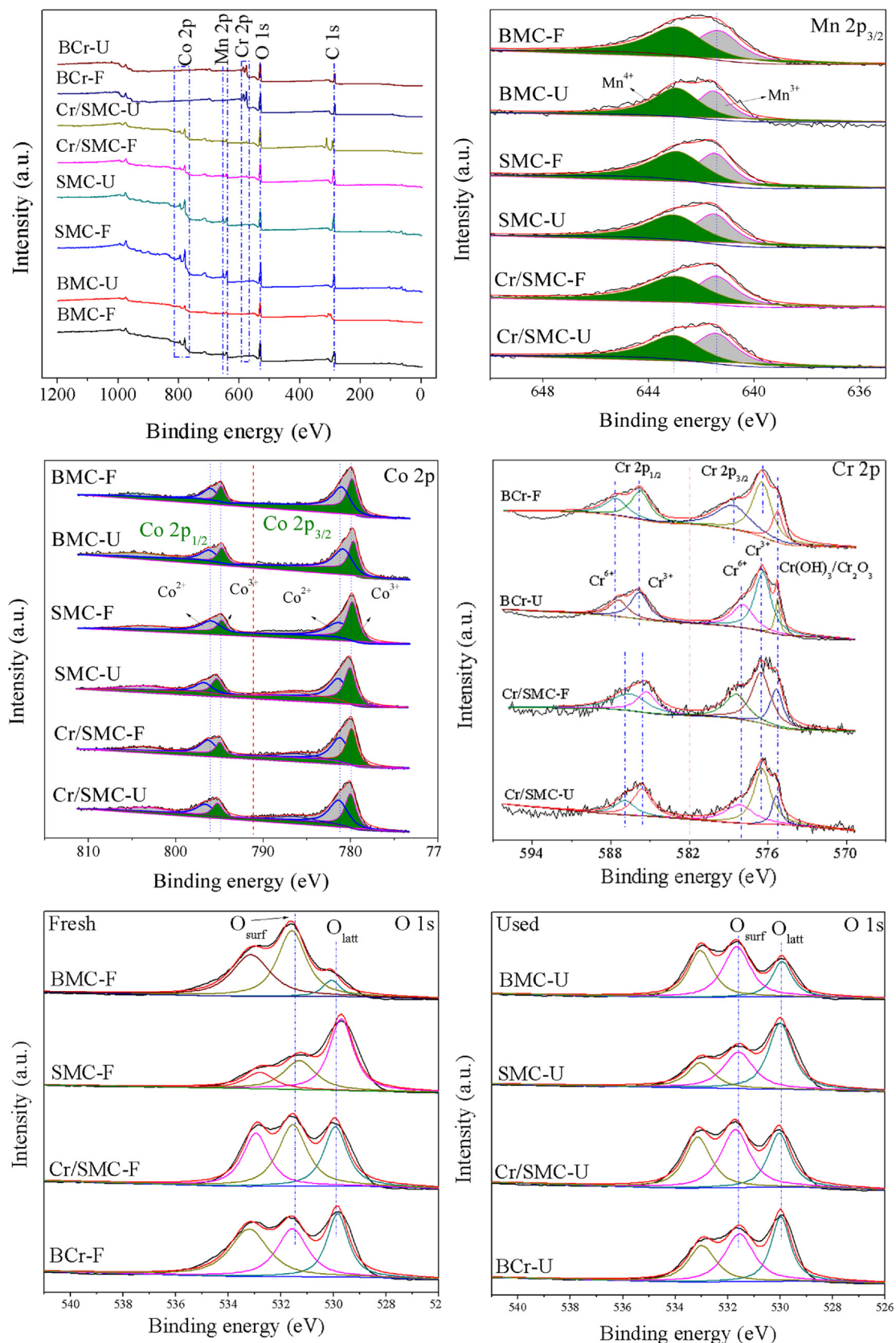
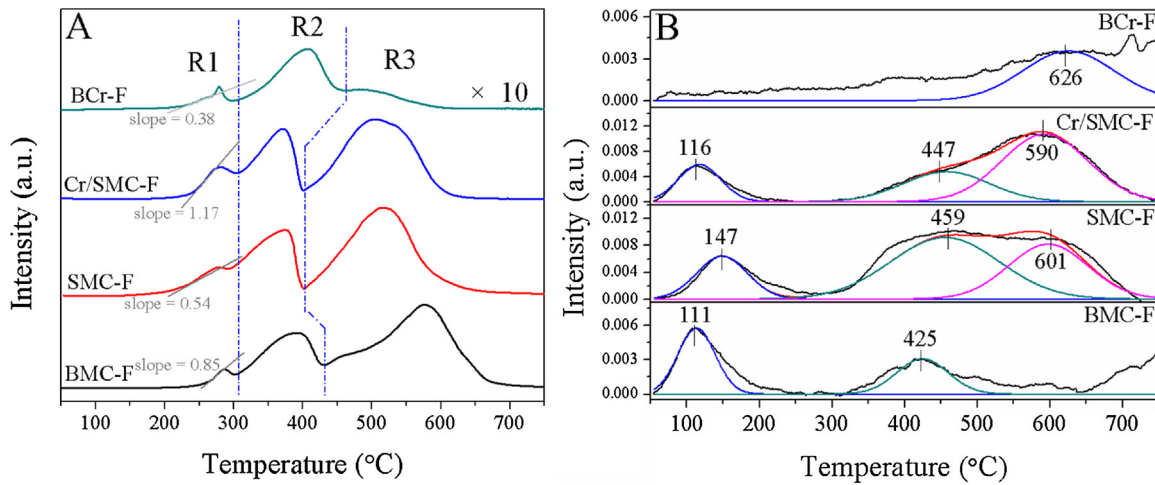


Fig. 5. XPS spectra of the fresh and used catalysts.

Table 2

XPS results of the fresh and used catalysts.

Sample	Binding energy (eV)								Molar ratio				
	Mn ³⁺	Mn ⁴⁺	Co ²⁺	Co ³⁺	Cr ₂ O ₃	Cr ³⁺	Cr ⁶⁺	O _{surf} ^a	O _{latt} ^b	Mn ⁴⁺ /Mn ³⁺	Co ³⁺ /Co ²⁺	Cr ⁶⁺ / (Cr ³⁺ + Cr ₂ O ₃)	O _{latt} /O _{surf}
BMC-F	641.6	643.2	796.0/781.0	794.8/779.8	/	/	/	531.6	530.1	1.21	1.74	/	0.15
SMC-F	641.2	642.6	796.0/781.3	794.7/779.8	/	/	/	531.3	529.7	1.32	1.81	/	1.85
Cr/SMC-F	641.4	642.9	796.3/781.2	794.9/779.8	575.5	576.7/587.8	578.6/585.9	531.6	529.9	1.35	1.83	0.62	0.77
BCr-F	/	/	/	/	575.3	576.4/587.7	578.6/585.9	531.6	529.9	/	/	0.58	0.91
BMC-U	641.0	642.5	796.2/780.8	794.7/779.7	/	/	/	531.7	530.0	1.38	1.60	/	0.51
SMC-U	641.5	643.0	796.8/781.4	795.3/780.0	/	/	/	531.6	530.0	1.18	2.05	/	1.40
Cr/SMC-U	641.4	643.0	796.6/781.3	795.2/780.0	575.3	576.5/587.0	578.1/585.6	531.1	530.0	0.97	2.01	0.56	0.70
BCr-U	/	/	/	/	575.2	576.4/587.0	578.3/585.7	531.6	530.0	/	/	0.49	0.87

^a Surface adsorbed oxygen species.^b Lattice oxygen species.**Fig. 6.** (A) H₂-TPR and (B) O₂-TPD profiles of prepared catalysts.

cations (Cr⁶⁺, Mn⁴⁺/Mn³⁺, or Co³⁺/Co²⁺) and the surface acidic hydroxyl group [46]. The CrO_x modification enhances the acidic strength and increases acidic concentration of SMC-F, which can be also observed from Fig. 7A [45]. In addition, the acidic concentration of NH₃ desorption peaks of prepared catalysts follows the order of Cr/SMC-F (524.28) > SMC-F (468.79) > BMC-F (209.38) > BCr-F (70.66), as shown in Table S2.

NH₃-IR profile in Fig. 7B showed that the bands in the region of 1500–1400 cm⁻¹ are corresponded to asymmetric and symmetric bending vibrations of NH⁴⁺ species adsorbed on Brønsted acid (denoted as B acid) sites [18]. The bonds centered at 1422 cm⁻¹ over the SMC-F and Cr/SMC-F materials correspond to B acid sites; the bonds at 1607, 1545, 1328, 1285 and 1226 cm⁻¹ ascribe to the exposure of Lewis acid (denoted as L acid) sites and the bonds in the range of 3500–2250 cm⁻¹ are attributed to the N–H stretching vibration in coordinated ammonia and ammonium ions [47,48]. As displayed in Fig. 7B (NH₃-IR), both L and B acid sites exist over the prepared catalysts, which can be also confirmed by the NH₃-TPD profiles because NH₃ desorption peaks observed at 120–350 °C in NH₃-TPD can be ascribed to the existence of both L and B acid sites over the catalysts [49]. For SMC-F, the incorporation of Cr species generates more L acid sites corresponding to the exposure of L acid sites bond at 1226 cm⁻¹ (Fig. 7B). However, B acid sites and L acid sites at 1422 and 1545 cm⁻¹ are occupied after adding CrO_x species. In addition, L acid sites are also detected at approximately 1606, 1588, 1574, 1450 and 1440 cm⁻¹ and B acid site can be also detected at approximately 1550 cm⁻¹ by Py-IR technology [10,49–51]. Results show that the incorporation of Cr species generates more L acid sites corresponding to the exposure of L acid sites bond at 1588 cm⁻¹, in consistent with NH₃-IR result.

CO₂ desorption capability is one of the primary factors that enhances the oxidation activity [52] and CO₂ desorption at low temperature could generally promote the catalytic reaction because of the rapid removal of CO₂, which is regarded as the main product of VOC combustion from surface/active sites of the catalysts [53]. As shown in Fig. 7C, both SMC-F and Cr/SMC-F samples exhibit two CO₂ desorption peaks. The first peaks of the two samples are at the temperature of 225 and 184 °C and the second are both at 431 °C. It can be deserved that the CO₂ desorption temperature of Cr/SMC-F shifts to lower temperatures after the addition of CrO_x species to the SMC-F, which indicates the better CO₂ removal capacity of Cr/SMC-F. Similarly, the first desorption temperature of BMC-F (204 °C) is lower than that of SMC-F, indicating higher CO₂ removal capacity of BMC-F at low temperature. However, BMC-F owns weak CO₂ desorption ability at high temperature, which maybe limit its oxidation activity.

3.5. Catalytic performance

3.5.1. Catalytic activity and stability

The catalytic activity and apparent activation energy (E_a) of prepared catalysts were examined for 1,2-DCE oxidation, as shown in Fig. 8. As displayed in Fig. 8A, the 1,2-DCE conversion over all catalysts increases consistently with the increasing of reaction temperature. It is worth noting that BCr-F and BCo-F perform higher activity than that of BMC-F in temperature range of 145–312 and 100–300 °C, respectively; while the opposite result can be found when further increase the reaction temperature. SMC-F has better catalytic activity than that of BMC-F and Cr/BMC-F. Cr/SMC-F exhibits the best catalytic activity for 1,2-DCE oxidation, based on the result of T_{90} (the temperature for 90%

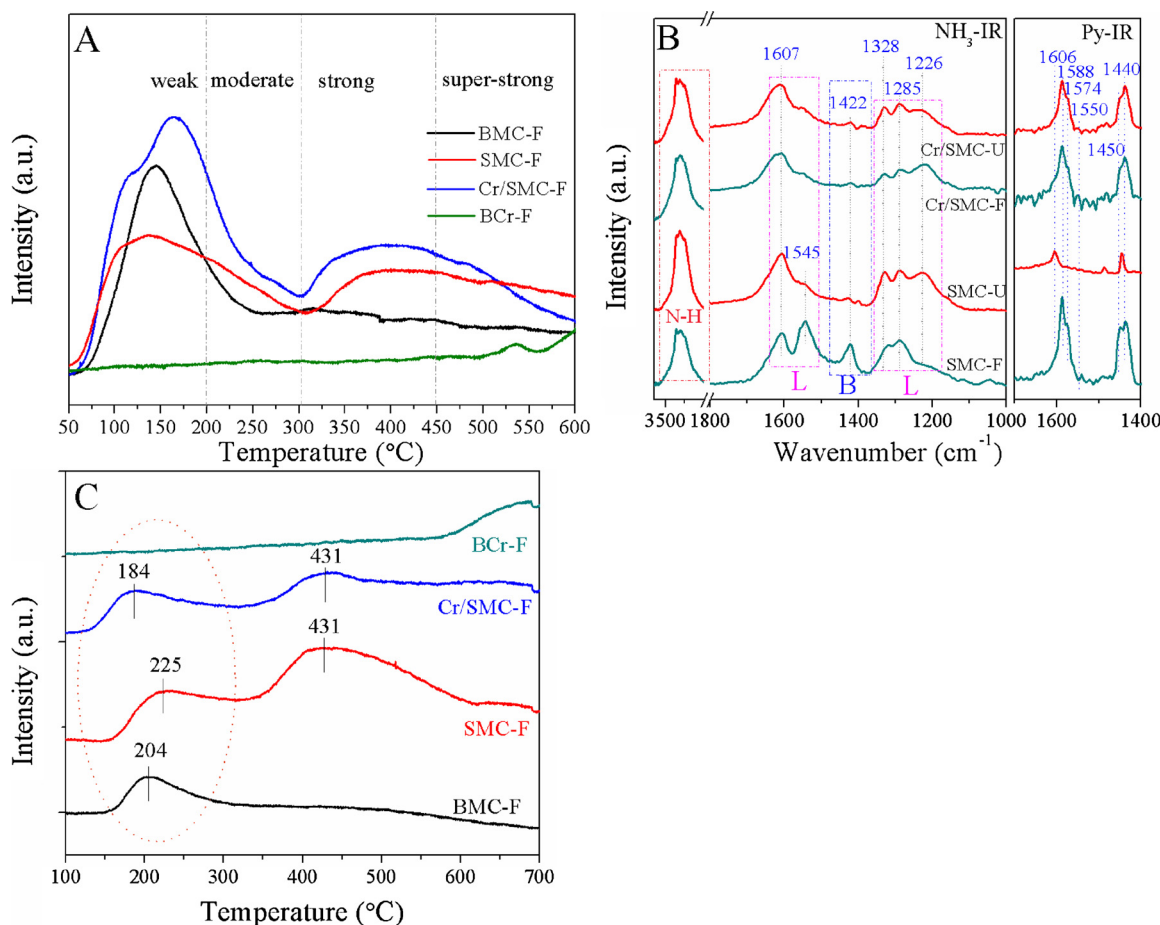


Fig. 7. (A) NH₃-TPD, (B) NH₃-IR/Py-IR and (C) CO₂-TPD profiles of prepared catalysts.

conversion of 1,2-DCE), the catalytic activity of prepared samples follows the sequence of Cr/SMC-F (266 °C) > SMC-F (296 °C) > Cr/BMC-F (324 °C) > BMC-F (339 °C) > BCr-F (345 °C) > BCo-F (383 °C). Table S1 summarizes the catalytic activity of some typical materials reported in previous works for the oxidation of 1,2-DCE. We can observed that the Cr/SMC-F sample almost owns the lowest T_{50} (177 °C) and the T_{90} temperature (266 °C) is also lower than the most of reported catalysts, demonstrating the superior oxidation performance of Cr/SMC-F for 1,2-DCE destruction.

The apparent activation energy of prepared catalysts in 1,2-DCE destruction was also calculated to further evaluate the catalytic performance, as displayed in Fig. 8B. It is widely accepted that the oxidation of 1,2-DCE under excess oxygen condition follows a first-order mechanism relating to 1,2-DCE concentration (c): $r = kc = (-Ae^{-E_a/RT})c$, where k , A , E_a , and r are rate constant (s^{-1}), pre-exponential factor, apparent activation energy (kJ/mol), and reaction rate ($\mu\text{mol g}^{-1} \text{s}^{-1}$), respectively. The E_a at low conversion (less than 20%) is estimated from the reaction rate in 1,2-DCE decomposition. As shown in Fig. 8B, the E_a values of the prepared catalysts obey the order of BMC-F (42.4 kJ mol⁻¹) > BCr-F (25.5 kJ mol⁻¹) > Cr/BMC-F (25.4 kJ mol⁻¹) > BCo-F (25.0 kJ mol⁻¹) > SMC-F (24.4 kJ mol⁻¹) > Cr/SMC-F (23.6 kJ mol⁻¹), indicating that Cr/SMC-F owns the best low-temperature 1,2-DCE destruction activity.

The yields of typical final oxidation products including CO_x (CO and CO₂), HCl and Cl₂ were further investigated, as depicted in Figs. 8C and S4. As shown in Fig. 8C, the temperature for total destruction of 1,2-DCE to CO₂ over prepared catalysts follows the sequence of BCr-F (> > 450 °C) > BCo-F (450 °C) > BMC-F (371 °C) > Cr/BMC-F (350 °C) > SMC-F (340 °C) > Cr/SMC-F (297 °C), suggesting that Cr/SMC-F has the best 1,2-DCE oxidation performance (carbon balance \geq

99.5%). In addition, to investigate the mineralization efficiency of the samples, the 1,2-DCE conversion as a function of CO₂ and CO_x yield (CO + CO₂) were also displayed in Fig. 8D. As shown in Fig. 8D (left), Cr/BMC-F, Cr/SMC-F and BCr-F catalysts own lower CO₂ selectivities compared with those of BMC-F, SMC-F and BCo-F materials at the same 1,2-DCE conversion (> 25%), which suggest that large amounts of CO or by-products generate during the oxidation process. However, Fig. 8D (right) reveals that Cr/BMC-F, Cr/SMC-F and BCr-F samples have superior CO_x selectivity, suggesting that CO instead of by-products generation over Cr-based materials occurs at relative low temperature during 1,2-DCE oxidation. Above results reveal that Cr/SMC-F has superior mineralization efficiency for 1,2-DCE destruction. HCl as the main inorganic chlorine product is detected and a small amount of Cl₂ is also found in the oxidation process, as depicted in Fig. S4. For the BCr-F sample, the yield of HCl increases persistently with the increasing of reaction temperature and reaches the highest value at about 400 °C; however, the yield of HCl over BCr-F slightly decreases from 84% to 80% when further increases the reaction temperature to 445 °C. The decrease of HCl yield indicates the occurrence of the Deacon reaction (2HCl (g) + 0.5O₂ → H₂O (g) + Cl₂ (g)) as HCl would be converted to Cl₂ at the temperature higher than 350 °C in the presence of O₂ [9], which can be also proved by the yield of Cl₂ (Fig. S4, insert) (chlorine balance achieves about 93–97%). Similar phenomenon can be observed over SMC-F and Cr/SMC-F catalysts.

The reaction stability of prepared catalysts and variation of oxidation by-products over SMC-F and Cr/SMC-F sample are studied, as displayed in Fig. 9A and B. In addition to this, the stability of the Cr/SMC-F in the oxidation of 1,2-DCE was further investigated in the co-existence of other typical VOC pollutant (toluene or methanol) to evaluate the catalytic performance in the oxidation of multi-component

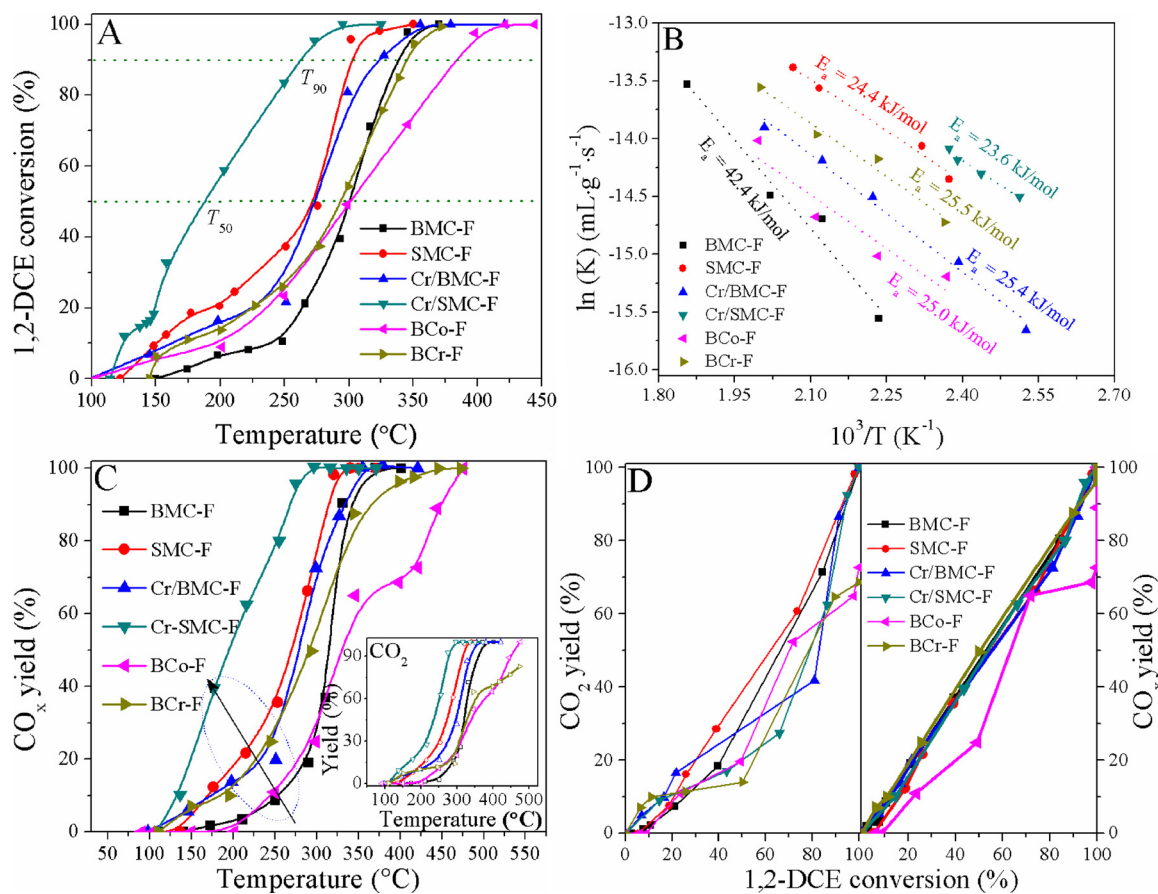


Fig. 8. (A) Catalytic activity, (B) apparent activation energy, (C) CO_x yield of prepared catalysts and (D) the relation between 1,2-dichloroethane conversion and CO₂/CO_x yield.

VOCs and further predicted its potential application prospect. As shown in Fig. 9A, BMC-F performs a good stability in the oxidation of 1,2-DCE at different reaction temperatures of 300 (T_{50}) and 340 °C (T_{100}) during the whole test period. Similarly, the 1,2-DCE conversion over SMC-F and Cr/SMC-F materials also keeps steady within the whole testing period (Figs. 9A and S7). However, the conversion of 1,2-DCE over BCr-F sample rapidly reduces from 80% to 66% when the oxidation reaction proceeds to 2.5 h and the conversion of 1,2-DCE further gradually reduces from 66% to 54% during the whole stability test due to the poor electron transfer ability of bulk CrO_x material during the oxidation reaction [20]. The crystal structure of the used samples was explored by XRD, as shown in Fig. 1B. The crystal phase of SMC-U and Cr/SMC-U is well maintained after the stability test, indicating the good structure stability and resistance to chlorine poisoning of these catalysts. However, several new diffraction peaks correspond to the diffraction of CrOCl (JCPDS No. 01-070-1658) can be found over BCr-U attributed to the attacking of Cl species to the crystal structure of BCr-F. Two diffraction peaks of BMC-U centered at 20 of 33.0 and 34.9° were deserved corresponding to the chlorinated framework (Co/MnCl_x or Co/MnO_yCl₂), which is indicated that the catalyst has Cl species deposition during 1,2-DCE destruction [54].

Fig. 9B shows the distribution of typical by-products (1,1,2-trichloroethane, trichloroethylene, perchloroethylene, trichloromethane and perchloromethane) as a function of reaction time over SMC-F and Cr/SMC-F catalysts in the stability tests. It is shown that the concentrations of all tested by-products over Cr/SMC-F are very stable and much lower than that over SMC-F sample. Remarkably, the variation of reaction by-products over SMC-F catalyst is much different from that of Cr/SMC-F. The concentration of 1,1,2-trichloroethane and trichloroethylene remains stable in the first 7 h and increases slowly

within the rest period of stability test. However, the concentration of perchloroethylene, trichloromethane and perchloromethane shows an increasing trend in the first 2 h and then remains stable in the time range of 2–16 h, which suggests SMC-F has lower by-product selectivity and reaction stability than that of Cr/SMC-F.

It is well known that industrial effluent streams contain a large variety of VOCs [55]. For example, 1,2-DCE, toluene and/or methanol are the common compounds existed in the stream of adhesive manufacturing and pharmaceutical industry [56,57]. Therefore, the catalytic oxidation behavior and stability of Cr/SMC-F in the oxidation of multiple VOCs were further investigated. The conversion of 1,2-DCE shows a decrease in catalytic activity from 90 to 79% with the addition of 1000 ppm of toluene, and a similar phenomenon can be observed when 1000 ppm of methanol is introduced (Fig. 9C and D) due to the competitive adsorption/oxidation between toluene/methanol and 1,2-DCE on active sites [58]. Interestingly, after toluene/methanol vapor is interrupted, the 1,2-DCE conversion recovered back to around 90% within half an hour. However, a slightly decrease of catalytic activity of Cr/SMC-F material can be observed in and without presence of toluene and methanol in the second cycle reaction, which is mainly due to more coke deposits on Cr/SMC-F material when high concentrations (1000 ppm) of methanol and toluene were injected.

3.5.2. Intermediate distribution and proposed mechanism

Several chlorinated by-products (1,1,2-trichloroethane, trichloroethylene, perchloroethylene, trichloromethane and perchloromethane) can be detected during 1,2-DCE destruction at different reaction temperatures, as displayed in Fig. S5. It is shown that just a small amount of 1,1,2-trichloroethane (1.8 ppm) was detected over BCr-F in temperature of 220–340 °C, suggesting the superior reaction

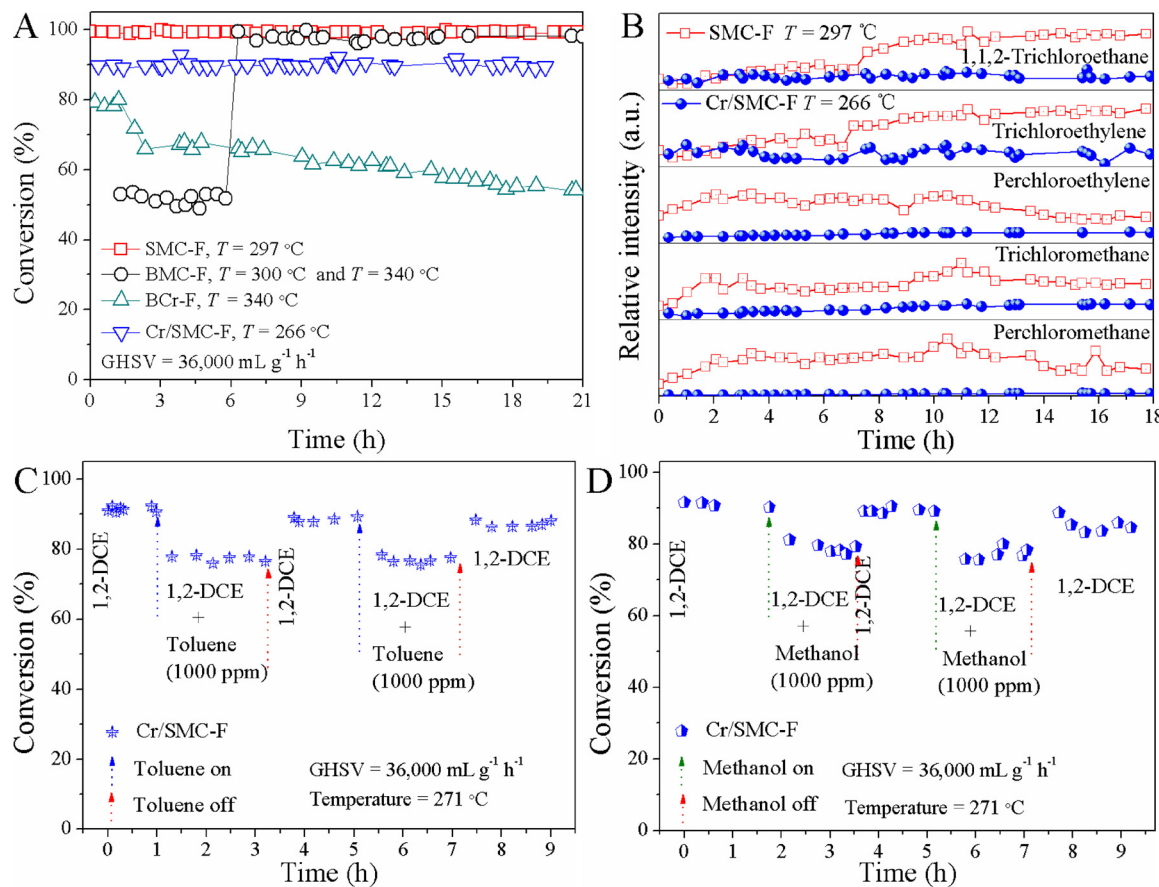


Fig. 9. (A) Stability of prepared materials for 1,2-DCE oxidation; (B) By-products distribution in the stability test over SMC-F and Cr/SMC-F; Reaction behaviors for 1,2-dichloroethane destruction in the presence of (C) toluene and (D) methanol over Cr/SMC-F material.

selectivity and total destruction capability of BCr-F material, in agreement with previous work [59]. 1,1,2-trichloroethane were detected over BMC-F, SMC-F and Cr/SMC-F materials at 160 °C and increases with the increasing of temperature, which respectively achieves the maximum values at round 227, 248 and 273 °C over Cr/SMC-F (31.8 ppm), SMC-F (42.4 ppm) and BMC-F (30.7 ppm) catalysts and then 1,1,2-trichloroethane would be oxidized to CO_x or other polychlorinated by-products. Interestingly, the trichloroethylene, trichloromethane and perchloromethane intermediates with similar trends as that of 1,1,2-trichloroethane can be only detected over BMC-F and SMC-F samples, indicating that the introduction of Cr species not only promotes the catalytic activity, but also inhibits the formation of reaction by-products due to the efficient Cl species removal ability of Cr element during 1,2-DCE decomposition. Perchloroethylene is only detected over BMC-F catalyst at a relatively high temperature range of 240–350 °C.

The variation of surface adsorbed species over BMC-F, SMC-F, Cr/SMC-F and BCr-F catalysts was studied via *in situ* DRIFTS, as shown in Fig. 10. The bands in 3350–3249 cm⁻¹ can be observed over all catalysts associating with the OH group vibration [60]. The intensity of these bands decreases with the increasing of temperature and achieves the minimum value at 200 °C. The bands in 1631–1625 cm⁻¹ are related to the stretching vibration of C=C, which decrease with the increasing of reaction temperature and almost disappear at 200 °C [61]. Two bands observed in 1544–1371 cm⁻¹ correspond to vibration of –CH₂–CH/–CH₃ groups or organic intermediates [10]. The bands at 1250–800 cm⁻¹ are attributed to the vibration of C–C bond [62]. For BMC-F and SMC-F catalysts, the intensity of C=C bond decreases with the increasing of temperature in 110–200 °C, indicating the cleavage of C=C bond. Moreover, three groups (–CH₂, –CH and –CH₃) on BMC-

F and SMC-F are detected at 170 °C, suggesting the formation of organic intermediates, in well consistent with the results of Fig. S5. In addition to this, the bond variations over BMC-F and SMC-F are almost the same, which indicates that the oxidation pathway of 1,2-DCE over these materials is essentially unchanged. After incorporation Cr element to SMC-F, the stretching vibration of C=C bond can be distinctly detected, while the stretching vibrations of –CH₂, –CH and –CH₃ groups are rather weak compared with that of BMC-F and SMC-F materials, indicating that the presence of Cr can achieve the deep oxidation of 1,2-DCE. Based on the results of by-products distribution (Fig. S5) and variation of surface adsorbed species, the reaction pathways over the synthesized catalysts were proposed, as displayed in Scheme 1. It is shown that the oxidation of 1,2-DCE over BMC-F and SMC-F materials follows a mechanism containing two decomposition paths, that is, 1,2-DCE is directly decomposed by C–Cl bond cleavage forming vinyl chloride, 1,1,2-trichloroethane, trichloroethylene and tetrachloroethylene (Path 1); 1,2-DCE is directly decomposed by C–C bond cleavage forming chloromethane, dichloromethane, trichloromethane and perchloromethane (Path 2). However, a different reaction mechanism which just includes Path 1 can be observed over Cr/SMC-F attributing to its excellent Cl species desorption capacity and high product selectivity. For BCr-F sample, 1,2-DCE can be almost directly oxidized to CO, CO₂, HCl and Cl₂, which follows the reaction way of Path 3.

3.5.3. Coke formation and chlorine resistance

TG-FTIR analysis was conducted to verify the coke formation and adsorbed species on the used catalysts, as shown in Fig. 11. Two weight loss regions can be observed over all used catalysts (Fig. 11A). The first weight loss region at temperature range of 50–200 °C is mainly ascribed

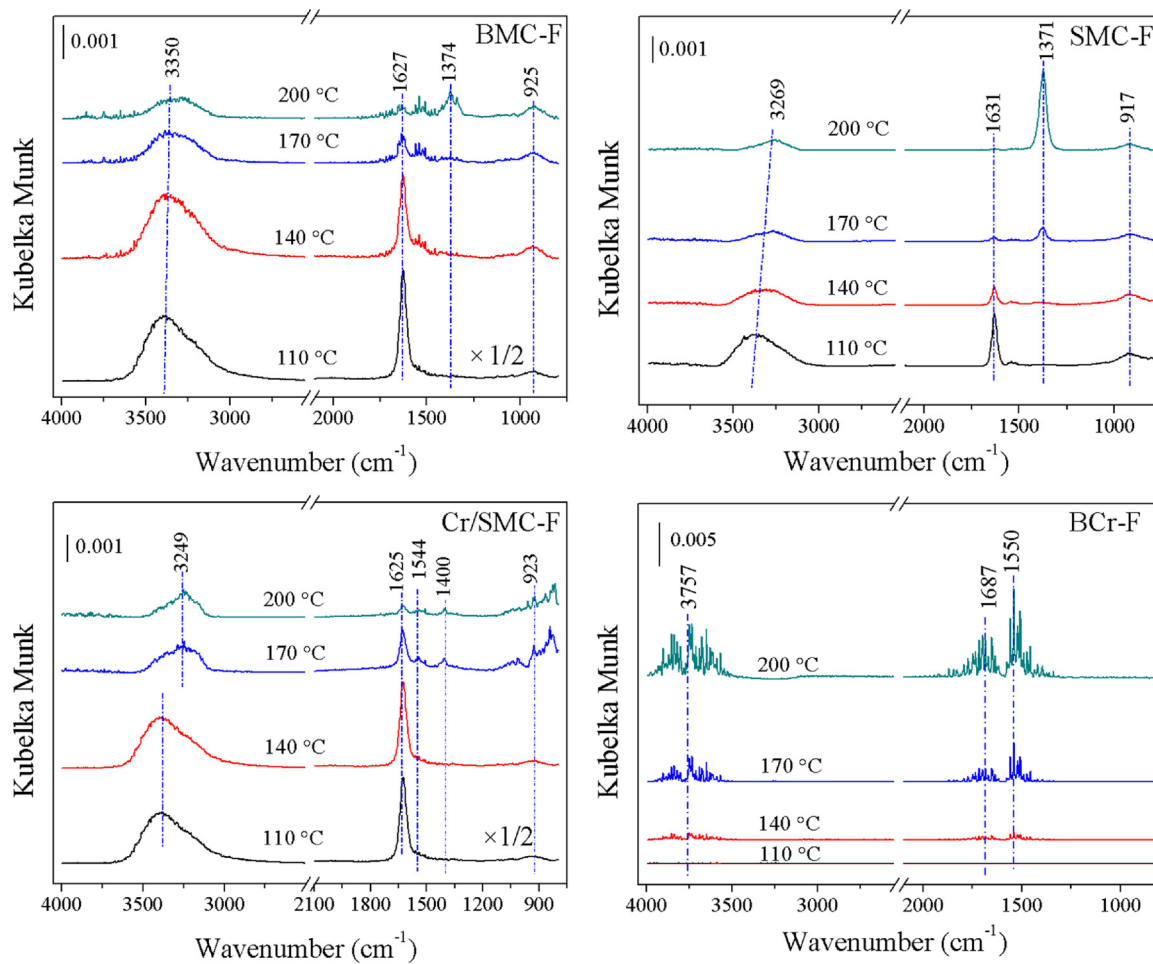
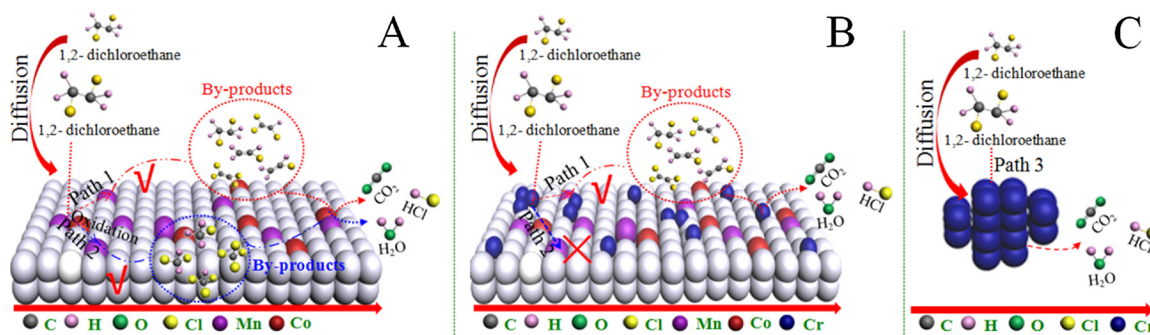


Fig. 10. *In situ* DRIFTS of 1,2-dichloroethane catalytic destruction over prepared catalysts.

to desorption of adsorbed molecular water, CO_2 , and organisms [63]. The second weight loss region at temperature range of 410–650 °C is usually assigned to the decomposition of coke deposits [8]. Corresponded to the TG results showed in Fig. 11A, the desorbed CO_2 was detected at 200 °C by *in situ* TG-FTIR. As shown in Fig. 11B, a small amount of CO_2 species can be observed when the temperature is higher than 400 °C, and no other species were detected. The total weight loss ratio of the used catalysts follows the order of BCr-U (0.46%) < BMC-U (1.79%) < Cr/SMC-U (4.59%) < SMC-U (6.25%).

O_2 -TPO-MS results in Fig. 12 reveal that the CO_2 formation and HCl desorption can be observed at 375 and 698 °C over SMC-U, respectively, which suggest that some coke deposition and HCl adsorption happen on SMC-U catalyst surface. No CO and Cl_2 are detected both on SMC-U and Cr/SMC-U materials. A MS signal associated to the formation of CO_2

during the oxidation of coke deposition is monitored at 390 °C over Cr/SMC-U; nevertheless, no HCl desorption peak appears, indicating the chlorine poisoning is slight or negligible due to the superior Cl removal ability of Cr/SMC-F. To investigate the chlorine deposit over catalysts, we further evaluate the Cl 2p XPS of the used catalysts, as shown in Fig. 13. Two peaks centered at 198.2–198.5 and 199.8–200.1 eV can be detected over SMC-U and Cr/SMC-U materials, which are respectively attributed to the HCl adsorption from 1,2-DCE decomposition and the adsorption of chlorinated organic species on catalyst surface [64]. Compared to SMC-U, Cr/SMC-U has a smaller amount of Cl species on the surface, which is related to the superior Cl species removal performance of Cr element, in agreement with the O_2 -TPO-MS results (Fig. 12).



Scheme 1. Proposed 1,2-dichloroethane destruction mechanism over prepared catalysts.

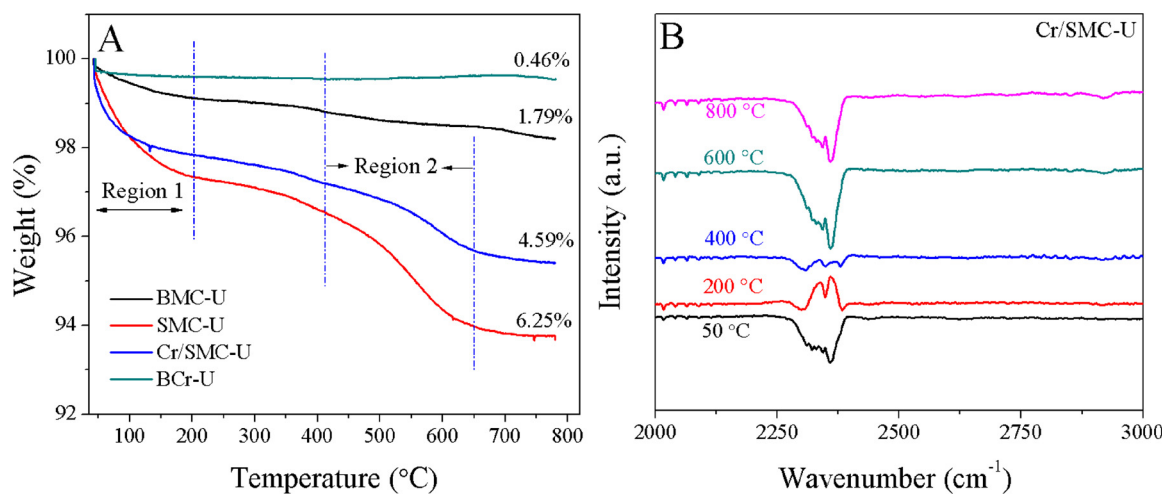


Fig. 11. (A) TG profiles of the used catalysts; (B) TG-FTIR patterns of Cr/SMC-U material.

3.5.4. Determining factor for 1,2-DCE destruction

In general, the catalytic performance of metal oxide catalysts is correlated with many factors including morphology, structural feature, element chemical state, redox property, acid property, and oxygen species distribution and mobility, which can be tuned by adjusting catalyst composition and preparation protocol. According to the results discussed previously, we found that the 3D porous system with large quantity of interconnected meso- and macro-pore channels is a kind of efficient structure for catalytic reactions considering its superior mass and heat transfer performance, especially for the reaction involved molecules with relative large diameter such as CVOCs and their derived organic by-products (Fig. 3) [29]. Furthermore, the 3D meso-macroporous structure of SMC-F owns superior structure stability because of no particle aggregation and structural distortion can be observed over SMC-U and Cr/SMC-U samples (Fig. 3f,i) after the stability test. However, BMC-U and BCr-U samples are severely sintered and lots of large aggregates formed (Fig. 3c, l), which suggest that the surfaces of BMC-F and BCr-U materials are probably attacked by chlorine species and/or coke in the oxidation process [20]. The results of nitrogen adsorption-desorption isotherms and BJH pore size distribution of the used samples also confirm that BMC-F and BCr-F samples occur surface sintering because of the slightly decrease of the specific surface area and pore volume of BMC-U and BCr-U samples (Fig. S3 and Table S4). The specific surface area of SMC-U increases because of the coke formation on the surface. As a consequence, the developed 3D meso-macroporous structure is beneficial for the reaction between SMC-F or Cr/SMC-F and

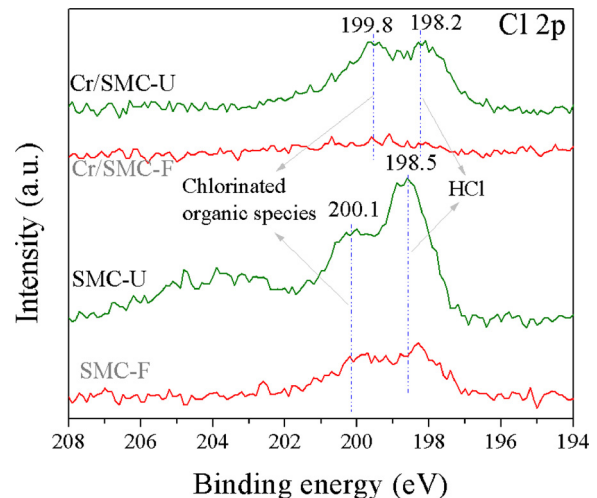


Fig. 13. Cl 2p XPS spectra of the used catalysts.

1,2-DCE. In comparison, the non-/limited porous structure can result in inferior catalytic performance of materials (e.g., BMC-F) (Figs. 3 and 4). However, the specific surface area is not the determining factor for the catalytic performance of prepared catalysts in the present work. For instance, the SMC-F sample with a higher specific surface area ($79.7 \text{ m}^2 \text{ g}^{-1}$) than that of Cr/SMC-F material ($52.4 \text{ m}^2 \text{ g}^{-1}$) performs a

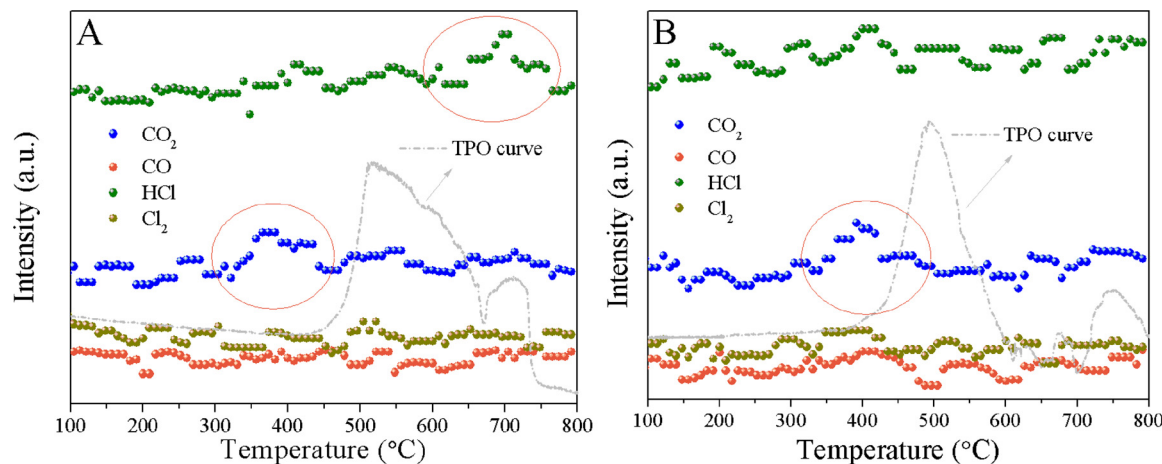


Fig. 12. O₂-TPO-MS profiles of (A) SMC-U and (B) Cr/SMC-U catalysts.

lower catalytic activity in 1,2-DCE destruction (Table 1).

Herein, the reducibility, oxygen species mobility and acid property are regarded as the most important factors for catalytic activity, reaction stability and chlorine/coke resistance in 1,2-DCE decomposition, demonstrating by results of XPS, H₂-TPR, O₂-TPD, CO₂-TPD, NH₃-TPD, NH₃-IR, O₂-TPO-MS and FTIR (Figs. 2, 5–7, and 13). In order to determine the redox center in the oxidation reaction, we analyzed the element status of the fresh and used materials. As shown in Table 2, Cr/SMC-F with the best catalytic activity has a lot of Cr⁶⁺ species (Cr⁶⁺/(Cr³⁺ + Cr₂O₃) = 0.62) and the ratios of Mn⁴⁺/Mn³⁺ (1.35) and Co³⁺/Co²⁺ (1.83) over which are slightly increased compared to those of SMC-F (respectively; 1.32 and 1.81), suggesting that the introduction of CrO_x promotes the generation of high valence Mn⁴⁺ and Co³⁺ species [20]. By comparing the surface status of the fresh and used catalysts, we find that the Cr⁶⁺/(Cr³⁺ + Cr₂O₃) ratios over Cr/SMC-F and BCr-F is slightly decreased from 0.62 and 0.58 to 0.56 and 0.49 after the reaction, respectively, and the Mn⁴⁺/Mn³⁺ ratios over SMC-F and Cr/SMC-F samples respectively decrease from 1.32 and 1.35 to 1.18 and 0.97, suggesting that a portion of Cr⁶⁺ and Mn⁴⁺ species considered as redox centers are reduced to Cr³⁺ and Mn³⁺ species and oxidize 1,2-DCE. Interestingly, the SMC-U and Cr/SMC-U own higher Co³⁺/Co²⁺ ratios (respectively; 2.05 and 2.01) than those of SMC-F (1.81) and Cr/SMC-F (1.83), suggesting that the electron transfer between different valence elements in the oxidation process promotes the oxidation of Co²⁺. The relationship between Mn⁴⁺/Mn³⁺ species and catalytic activity is displayed in Fig. S6. The catalysts (BMC-F, SMC-F and Cr/SMC-F) with higher Mn⁴⁺/Mn³⁺ ratio (respectively; 1.21, 1.32 and 1.35) possess lower *T*₉₀ (339, 296 and 266 °C), indicating that the highly reducible Mn⁴⁺ species are closely related to the activity of prepared materials.

Oxygen species are generally regarded as an important role in 1,2-DCE destruction for balancing the surface charge and maintaining redox reaction cycle [65]. O 1s XPS results of the used samples show that the O 1s core levels of surface lattice oxygen species over all the used catalysts shift to higher binding energy values owing to the “O → Co”, “O → Co” or “O → Mn” electron-transfer process, creating active oxygen species such as O[·], O²⁻, and O⁻, compared with the fresh catalysts [66]. The reduced Cr/Mn elements during 1,2-DCE oxidation would be oxidized by the relevant oxygen species (O[·], O²⁻, and O⁻) to restore the oxidation property of materials. The significant decrease trend of O_{latt}/O_{surf} ratios of SMC-U (1.40), Cr/SMC-U (0.70) and BCr-U (0.87) compared to SMC-F (1.85), Cr/SMC-F (0.77) and BCr-F (0.91), indicating that lattice oxygen species over these catalysts play a dominant role in the oxidation of 1,2-DCE. Thus, the mobility of lattice oxygen species is regarded as a critical factor in 1,2-DCE destruction in this work. O₂-TPD results suggest that the surface lattice oxygen species of Cr/SMC-F owns lower desorption temperature (590 °C) and relatively larger peak area (0.231) than that of SMC-F (601 °C and 0.162), indicating that Cr/SMC-F owns higher surface lattice oxygen species mobility than that of SMC-F and the incorporation of CrO_x promotes the mobility of surface lattice oxygen species. Partial surface lattice oxygen species are consumed during the long term stability test, the Cr⁶⁺-O peak (938 cm⁻¹) of Cr/SMC-U disappears after the oxidation reaction compared to Cr/SMC-F, indicating that Cr⁶⁺-O species are reduced to Cr³⁺-O (655 cm⁻¹) and the surface lattice oxygen species are expended by 1,2-DCE/by-products, which can be clearly observed in FTIR result (Fig. 2C) [67]. Therefore, the better catalytic performance of Cr/SMC-F than SMC-F can be owing to the easier desorbed surface lattice oxygen species and enrichment highly reducible Cr⁶⁺, Mn⁴⁺ and Co³⁺ cations. It is worth noting that a large amount of by-products produces on the Lewis acid sites of SMC-F resulting in the increase of L acid sites intensity on SMC-F (observed over SMC-U) in 1,2-DCE destruction process, in agreement with the Cl 2p XPS results (Fig. 13). The modification of SMC-F by CrO_x addition drastically inhibits by-products formation because of the superior CO₂ and Cl desorption performance of CrO_x, which is confirmed by results of by-products distribution, CO₂-TPD, O₂-TPO-MS and Cl XPS (Figs. 7, 12 and 13). Additionally, the

presence of CrO_x occupies the Brønsted acid sites and increases the acid strength of SMC-F, leading to the main exposure of Lewis acid sites in Cr/SMC-F. The unchanged Brønsted acid sites exposure of Cr/SMC-U compared with Cr/SMC-F also suggests the excellent Cl desorption performance of Cr/SMC-F, which is a key point of reaction stability and selectivity (Fig. 7B) [36]. However, it is interesting to observe that the B acid sites of SMC-F at 1422 cm⁻¹ disappear (Fig. 7B) due to the adsorption of Cl species, and the L acid sites at 1545 cm⁻¹ also changes little. It can be concluded that the Cl dissociative adsorption and the weak C-Cl bonds rupture take place on the L acid sites of Cr/SMC-F sample, but both L and B acid sites work in 1,2-DCE destruction. In short, the strong oxide species (Cr⁶⁺) and highly removable surface lattice oxygen species can enhance the catalytic activity and increase CO₂ selectivity (Fig. 8C) of the sample, and the L and B acid sites of Cr/SMC-F can efficiently remove Cl species from the material surface (Cl XPS, Fig. 13) and thus improve the reaction stability.

4. Conclusions

In this work, a 3D nanosphere-like meso-macroporous SMC-F material with particle size about 240 nm was firstly prepared *via* a co-precipitation method and CrO_x component is introduced by a rotary evaporation method for synthesizing Cr/SMC-F catalyst, which is a robust composite catalyst for 1,2-DCE destruction. Results show that SMC-F and Cr/SMC-F materials with 3D meso-macroporous structure own better catalytic activity and selectivity than BMC-F. On line analysis and *in situ* FTIR results reveal that a large amount of by-products, such as 1,1,2-trichloroethane, trichloroethylene, perchloroethylene, trichloromethane and perchloromethane, produced over SMC-F in 1,2-DCE decomposition process, which would lead to Cl poisoning of catalysts. The by-products formation mechanism confirmed by the *in situ* FTIR results includes the cleavage of C-Cl bond, the cleavage of C-C bond and the formation of C-H bond. The addition of CrO_x greatly improves the catalytic activity and selectivity of SMC-F and obviously inhibits the formation of polychlorinated by-products attributed to the higher Cr⁶⁺ and Mn⁴⁺/Mn³⁺ ratio, superior O²⁻ mobility capacity and excellent Cl removal capacity of Cr/SMC-F. Only 1,1,2-trichloromethane can be detected over Cr/SMC-F in 1,2-DCE destruction and all detected by-products over BMC-F, SMC-F and Cr/SMC-F are totally oxidized to CO, CO₂, HCl and Cl₂. Importantly, Cr/SMC-F owns excellent catalytic stability due to its high removal capability for Cl species. It can be anticipated that the Cr/SMC-F material with superior catalytic performance and chlorine resistance is a promising candidate for CVOC destruction.

Declaration of Competing Interest

The authors declare that they have no known competing financial interests or personal relationships that could have appeared to influence the work reported in this paper.

Acknowledgements

This work was financially supported by National Natural Science Foundation of China (21677114, 21876139, 21477095), the Key R&D Program of Shaanxi Province (2019SF-244, 2019ZDLSF05-05-02), the National Key R&D Program of China (2016YFC0204201), and the Fundamental Research Funds for the Central Universities (xjj2017170). The authors also appreciate the editor and reviewers for their professional work and valuable comments.

Appendix A. Supplementary data

Supplementary material related to this article can be found, in the online version, at doi:<https://doi.org/10.1016/j.apcatb.2019.118018>.

References

[1] J. Chen, X. Chen, X. Chen, W. Xu, Z. Xu, H. Jia, J. Chen, *Appl. Catal. B: Environ.* 224 (2018) 825–835.

[2] P. Yang, S. Fan, Z. Chen, G. Bao, S. Zuo, C. Qi, *Appl. Catal. B: Environ.* 239 (2018) 114–124.

[3] C. He, J. Cheng, X. Zhang, M. Douthwaite, S. Pattisson, Z. Hao, *Chem. Rev.* 119 (2019) 4471–4568.

[4] M. Piutmetti, D. Fino, N. Russo, *Appl. Catal. B: Environ.* 163 (2015) 277–287.

[5] Z. Boukha, J. González-Prior, B. de Rivas, J.R. González-Velasco, R. López-Fonseca, J.I. Gutiérrez-Ortiz, *Appl. Catal. B: Environ.* 190 (2016) 125–136.

[6] P. Yang, S. Zuo, Z. Shi, F. Tao, R. Zhou, *Appl. Catal. B: Environ.* 191 (2016) 53–61.

[7] Z. El Assal, S. Ojala, S. Pitkäaho, L. Pirault-Roy, B. Darif, J.-D. Comparat, M. Bensitel, R.L. Keiski, R. Brahmi, *Chem. Eng. J.* 313 (2017) 1010–1022.

[8] M. Tian, M. Ma, B. Xu, C. Chen, C. He, Z. Hao, R. Albilali, *Catal. Sci. Technol.* 8 (2018) 4503–4514.

[9] M. Tian, C. He, Y. Yu, H. Pan, L. Smith, Z. Jiang, N. Gao, Y. Jian, Z. Hao, Q. Zhu, *Appl. Catal. A Gen.* 553 (2018) 1–14.

[10] T. Cai, H. Huang, W. Deng, Q. Dai, W. Liu, X. Wang, *Appl. Catal. B: Environ.* 166–167 (2015) 393–405.

[11] P. Yang, S. Yang, Z. Shi, Z. Meng, R. Zhou, *Appl. Catal. B: Environ.* 162 (2015) 227–235.

[12] J. Gonzalez-Prior, R. Lopez-Fonseca, J.I. Gutierrez-Ortiz, B. de Rivas, *Appl. Catal. B: Environ.* 199 (2016) 384–393.

[13] C. Shi, Y. Wang, A. Zhu, B. Chen, C. Au, *Catal. Commun.* 28 (2012) 18–22.

[14] X. Wang, K. Qian, L. Dao, *Appl. Catal. B: Environ.* 86 (2009) 166–175.

[15] W. Tang, X. Wu, S. Li, W. Li, Y. Chen, *Catal. Commun.* 56 (2014) 134–138.

[16] B. Faure, P. Alphonse, *Appl. Catal. B: Environ.* 180 (2016) 715–725.

[17] J. González-Prior, R. López-Fonseca, J.I. Gutiérrez-Ortiz, B. de Rivas, *Appl. Catal. B: Environ.* 222 (2018) 9–17.

[18] C. He, Z. Jiang, M. Ma, X. Zhang, M. Douthwaite, J. Shi, Z. Hao, *ACS Catal.* 8 (2018) 4213–4229.

[19] Z. Jiang, C. He, N.F. Dummer, J. Shi, M. Tian, C. Ma, Z. Hao, S.H. Taylor, M. Ma, Z. Shen, *Appl. Catal. B: Environ.* 226 (2018) 220–233.

[20] M. Tian, Y. Jian, M. Ma, C. He, C. Chen, C. Liu, J.-W. Shi, *Appl. Catal. A Gen.* 570 (2019) 62–72.

[21] Y. Jian, M. Ma, C. Chen, C. Liu, Y. Yu, Z. Hao, C. He, *Catal. Sci. Technol.* 8 (2018) 3863–3875.

[22] M.D. Ma, H. Huang, C.W. Chen, Q. Zhu, L. Yue, R. Albilali, C. He, *Mol. Catal.* 455 (2018) 192–203.

[23] Y. Jian, T. Yu, Z. Jiang, Y. Yu, M. Douthwaite, J. Liu, R. Albilali, C. He, *ACS Appl. Mater. Interf.* 11 (2019) 11369–11383.

[24] Z. Jiang, X. Feng, J. Deng, C. He, M. Douthwaite, Y. Yu, J. Liu, Z. Hao, Z. Zhao, *Adv. Funct. Mater.* (2019) 1902041.

[25] Q. Dai, S. Bai, H. Li, W. Liu, X. Wang, G. Lu, *Appl. Catal. B: Environ.* 168 (2015) 141–155.

[26] Q. Chen, Q. Wu, *J. Hazard. Mater.* 283 (2015) 193–201.

[27] L. Dong, Y. Jin, T. Song, J. Liang, X. Bai, S. Yu, C. Teng, X. Wang, J. Qu, X. Huang, *Environ. Sci. Pollut. Res. Int.* 24 (2017) 17626–17641.

[28] B.M. Abu-Zied, *Appl. Catal. A Gen.* 198 (2000) 139–153.

[29] X. Hu, L. Huang, J. Zhang, H. Li, K. Zha, L. Shi, D. Zhang, J. Mater. Chem. A 6 (2018) 2952–2963.

[30] C. Chen, H. Huang, Y. Yu, J. Shi, C. He, R. Albilali, H. Pan, *Chem. Eng. J.* 353 (2018) 584–594.

[31] P. Xiao, J. Zhu, H. Li, W. Jiang, T. Wang, Y. Zhu, Y. Zhao, J. Li, *ChemCatChem* 6 (2014) 1774–1781.

[32] L. Wang, X. Cheng, Z. Wang, C. Ma, Y. Qin, *Appl. Catal. B: Environ.* 201 (2017) 636–651.

[33] J.N. Kondo, M. Uchida, K. Nakajima, D.L. Lu, M. Hara, K. Domen, *Chem. Mater.* 16 (2004) 4304–4310.

[34] Y. Su, Z. Tang, W. Han, Y. Song, G. Lu, *Catal. Surv. Asia* 19 (2015) 68–77.

[35] W. Yang, Y. Zhu, F. You, L. Yan, Y. Ma, C. Lu, P. Gao, Q. Hao, W. Li, *Appl. Catal. B: Environ.* 233 (2018) 184–193.

[36] X. Weng, P. Sun, Y. Long, Q. Meng, Z. Wu, *Environ. Sci. Technol.* 51 (2017) 8057–8066.

[37] T.-T. Zhang, J.-D. Song, J.-X. Chen, A.-P. Jia, M.-F. Luo, J.-Q. Lu, *Appl. Surf. Sci.* 425 (2017) 1074–1081.

[38] J. Zhu, H. Li, L. Zhong, P. Xiao, X. Xu, X. Yang, Z. Zhao, J. Li, *ACS Catal.* 4 (2014) 2917–2940.

[39] P. Yang, S. Zuo, R. Zhou, *Chem. Eng. J.* 323 (2017) 160–170.

[40] W. Tang, W. Xiao, S. Wang, Z. Ren, J. Ding, P.-X. Gao, *Appl. Catal. B: Environ.* 226 (2018) 585–595.

[41] H. Pan, Y. Jian, C. Chen, C. He, Z. Hao, Z. Shen, H. Liu, *Environ. Sci. Technol.* 51 (2017) 6288–6297.

[42] Z. Shi, P. Yang, F. Tao, R. Zhou, *Chem. Eng. J.* 295 (2016) 99–108.

[43] X. Chen, X. Chen, E. Yu, S. Cai, H. Jia, J. Chen, P. Liang, *Chem. Eng. J.* 344 (2018) 469–479.

[44] J. Su, W. Yao, Y. Liu, Z. Wu, *Appl. Surf. Sci.* 396 (2017) 1026–1033.

[45] Z. Zhang, J. Huang, H. Xia, Q. Dai, Y. Gu, Y. Lao, X. Wang, *J. Catal.* 360 (2018) 277–289.

[46] Q. Dai, Z. Zhang, J. Yan, J. Wu, G. Johnson, W. Sun, X. Wang, S. Zhang, W. Zhan, *Environ. Sci. Technol.* 52 (2018) 13430–13437.

[47] Q. Zhang, Y. Tan, G. Liu, J. Zhang, Y. Han, *Green Chem.* 16 (2014) 4708–4715.

[48] M. Casapu, O. Kroeker, M. Mehring, M. Nachtegaal, C. Borca, M. Harfouche, D. Grolimund, *J. Phys. Chem. C* 114 (2010) 9791–9801.

[49] H. Chang, M. Jong, C. Wang, R. Qu, Y. Du, J. Li, J. Hao, *Environ. Sci. Technol.* 47 (2013) 11692–11699.

[50] Z. Zhang, H. Xia, Q. Dai, X. Wang, *Appl. Catal. A Gen.* 557 (2018) 108–118.

[51] X. Yang, F. Wang, R. Wei, S. Li, Y. Wu, P. Shen, H. Wang, L. Gao, G. Xiao, *Microp. Mesop. Mat.* 257 (2018) 154–161.

[52] C. He, J. Li, X. Zhang, L. Yin, J. Chen, S. Gao, *Chem. Eng. J.* 180 (2012) 46–56.

[53] Q. Dai, Q. Zhu, Y. Lou, X. Wang, *J. Catal.* 357 (2018) 29–40.

[54] W.L. Wang, Q. Meng, Y. Xue, X. Weng, P. Sun, Z. Wu, *J. Catal.* 366 (2018) 213–222.

[55] B. Huang, C. Lei, C. Wei, G. Zeng, *Environ. Int.* 71 (2014) 118–138.

[56] M.R. Gwinn, D.O. Johns, T.F. Bateson, K.Z. Guyton, *Mutat. Res./Rev. Mutat.* 727 (2011) 42–53.

[57] X.H. Zhang, Q.L. Liu, Y. Xiong, A.M. Zhu, Y. Chen, Q.G. Zhang, *J. Membrane Sci.* 327 (2009) 274–280.

[58] J. Bedia, A. Arevalo-Bastante, J.M. Grau, L.A. Dosso, J.J. Rodriguez, A. Mayoral, I. Diaz, L.M. Gómez-Sainero, *J. Catal.* 352 (2017) 562–571.

[59] P. Yang, Z. Shi, F. Tao, S. Yang, R. Zhou, *Chem. Eng. Sci.* 134 (2015) 340–347.

[60] J. Wu, Q. Xia, H. Wang, Z. Li, *Appl. Catal. B: Environ.* 156–157 (2014) 265–272.

[61] P.S. Chintawar, H.L. Greene, *J. Catal.* 165 (1997) 12–21.

[62] C. He, Y. Yu, J. Shi, Q. Shen, J. Chen, H. Liu, *Mater. Chem. Phys.* 157 (2015) 87–100.

[63] C. Chen, Y. Yu, C. He, L. Wang, H. Huang, R. Albilali, J. Cheng, Z. Hao, *Appl. Surf. Sci.* 439 (2018) 113–121.

[64] Q. Dai, S. Bai, J. Wang, M. Li, X. Wang, G. Lu, *Appl. Catal. B: Environ.* 142 (2013) 222–233.

[65] Y. Zheng, K. Li, H. Wang, Y. Wang, D. Tian, Y. Wei, X. Zhu, C. Zeng, Y. Luo, *J. Catal.* 344 (2016) 365–377.

[66] C. He, Y. Yu, Q. Shen, J. Chen, N. Qiao, *Appl. Surf. Sci.* 297 (2014) 59–69.

[67] B.M. Abu-Zied, T.T. Ali, *Appl. Surf. Sci.* 457 (2018) 1126–1135.